Sea-ice melt onset associated with lead opening during the spring/summer transition near the North Pole

Frédéric Vivier, Jennifer K. Hutchings, Yusuke Kawaguchi, Takashi Kikuchi, James H. Morison, Antonio Lourenço, Tomohide Noguchi

RESEARCH ARTICLE

Key Points:
- Sea ice melt onset at the North Pole documented from a set of autonomous buoys
- Basal melt rate is consistent with absorption of solar radiations at leads
- Processes controlling basal melt and mixed-layer warming are investigated from a 1-D model

Correspondence to:
F. Vivier,
frederic.vivier@locean-ipsl.upmc.fr

Sea ice melt onset associated with lead opening during the spring/summer transition near the North Pole

Frédéric Vivier[1], Jennifer K. Hutchings[2], Yusuke Kawaguchi[3], Takashi Kikuchi[3], James H. Morison[4], Antonio Lourenço[1], and Tomohide Noguchi[5]

[1]Laboratoire d'Océanographie et du Climat: Expérimentation et Approches Numériques, Institut Pierre-Simon Laplace, CNRS, Sorbonne Universités (UPMC Paris 6), Paris, France, [2]College of Earth, Ocean and Atmospheric Sciences, Oregon State University, Corvallis, Oregon, USA, [3]Research Institute of Global Change, Japan Agency for Marine-Earth Science and Technology, Yokosuka, Japan, [4]Polar Science Center, University of Washington, Seattle, Washington, USA, [5]Marine Works Japan Ltd., Yokohama, Japan

Abstract In the central Arctic Ocean, autonomous observations of the ocean mixed layer and ice documented the transition from cold spring to early summer in 2011. Ice-motion measurements using GPS drifters captured three events of lead opening and ice ridge formation in May and June. Satellite sea ice concentration observations suggest that locally observed lead openings were part of a larger-scale pattern. We clarify how these ice deformation events are linked with the onset of basal sea ice melt, which preceded surface melt by 20 days. Observed basal melt and ocean warming are consistent with the available input of solar radiation into leads, once the advent of mild atmospheric conditions prevents lead refreezing. We use a one-dimensional numerical simulation incorporating a Local Turbulence Closure scheme to investigate the mechanisms controlling basal melt and upper ocean warming. According to the simulation, a combination of rapid ice motion and increased solar energy input at leads promotes basal ice melt, through enhanced mixing in the upper mixed layer, while slow ice motion during a large lead opening in mid-June produced a thin, low-density surface layer. This enhanced stratification near the surface facilitates storage of solar radiation within the thin layer, instead of exchange with deeper layers, leading to further basal ice melt preceding the upper surface melt.

1. Introduction

Increasingly early Arctic sea ice melt onset [*Markus et al.*, 2009] enhances summer melt, through amplification by the albedo feedback [*Perovich et al.*, 2011]. The timing of sea ice surface melt onset displays large geographical and interannual variability. In the central Arctic, it occurs around day of year 175 with a standard deviation of 5 days [*Markus et al.*, 2009]. To date, the majority of information about sea ice melt onset timing is from satellite remote sensing, which detects changes of the upper ice surface, while summer ice melt occurs not only through surface ablation, but also through basal melt and lateral melt at lead edges. The partitioning between lateral and vertical melt is often assumed in models. According to *Steele* [1992], lateral melt is important in the mass balance for floe sizes less than 30 m: we therefore do not expect it to be a major contributor in the central Arctic at the time of melt onset. The relative contributions to ice melt from basal and surface melt vary geographically [*Perovich et al.*, 2011], with larger basal melt in the Greenland Sea for example. In many locations, including the near North Pole location discussed in this paper [*Richter-Menge et al.*, 2006, Table 1], compared to surface melt, basal melt has equal or higher contribution to total ice melt [*Perovich et al.*, 2011], and basal melt ultimately contributes to ice area reduction. We expect that variability in the onset of basal melt is an important component of the variability and trends in albedo feedback and the Arctic wide sea ice mass balance. As differing processes control the onset of basal melt and surface melt, we do not expect that these are tightly coordinated in time. To our knowledge, the variability in the onset of basal melt timing is not known. The onset of basal melt depends on the relative magnitude of the conductive heat fluxes within the ice and the magnitude of the ocean/ice interface heat fluxes, F_w [e.g., *Maykut and Untersteiner*, 1971]. *Shaw et al.* [2009] showed a good agreement between F_w and observed bottom ablation rates from data collected as part of the Surface Heat Budget of the Arctic Ocean (SHEBA) experiment in the late 1990s. Previous works by *Maykut and McPhee* [1995] showed that the

magnitude of F_w is linked with the solar heat input through open leads and thin ice. More recently, *Krishfield and Perovich* [2005] estimated F_w from automated buoys drifting in the western and central Arctic, finding that the variability in upper ocean heat content can be related to the local solar zenith angle. Likewise, in the central Arctic, *Stanton et al*. [2012] calculated F_w from upper ocean measurements obtained from autonomous systems repeatedly deployed in the Arctic Ocean Transpolar Drift between 2002 and 2010, finding that F_w is primarily supported by local radiative energy flux entering the upper ocean through areas of open water. However, as shown by *Hayes and Morison* [2008] both from observations collected during SHEBA and numerical modeling, the way thermal energy enters the ocean mixed layer in summertime and interacts with the surface highly depends on turbulent boundary layer processes.

In this paper, we investigate the processes controlling the onset of basal ice melt during the drift of an array of autonomous buoys. For the array, we estimate the heat budget in the upper ocean during the transition between basal ice growth and melt. Ice drifting buoy data demonstrate a link between deformation of the ice pack, lead opening, and the commencement of basal ice melt in early summer. This suggests that the onset of basal melt depends upon the timing of wind-driven lead opening once the solar angle allows heating of open leads, but also on the advent of mild atmospheric conditions that prevent rapid lead refreezing, which would hamper penetration of solar radiation. Quiescent ice conditions, following lead opening, promote heating near the ocean surface contributing to build up a shallow stratification which enables enhanced ice melt as soon as turbulent mixing picks up.

We describe our observation program, which was part of the North Pole Environmental Observatory (NPEO) project [*Morison et al*., 2002], in section 2. In section 3, temporal changes of ice thickness, buoy array motion, and hydrographical properties are presented and discussed with special focus on three ridging/closing events. A simple heat and salt budget of the sea ice and ocean mixed layer, using surface forcing based on atmospheric reanalyses and satellite data is undertaken in section 4 to shed light on in situ observations. In section 5, a one-dimensional mixed-layer model, following *McPhee* [1999], using NPEO data as initial conditions and for some of the boundary conditions, is applied to our problem to investigate ocean mixed-layer dynamics in more detail. Finally, section 6 summarizes this paper.

2. Data

As part of the NPEO campaign, an array of ice drifting buoys was deployed near the geographic North Pole at (89.3°N, 142.4°E) on 12 April 2011, corresponding to day of year (DoY) 102 (Figure 1).

2.1. Ice-T Buoy

The array included an "Ice-T" (Ice-Thickness) buoy, which records parameters relevant to the local sea ice mass balance. The Ice-T includes a 2 m long floating surface buoy (hence adapted as well to seasonal ice), trapped in the ice, and an instrumented subsurface module hanging 6 m below the ice base, referred to as "the fish" hereinafter. The surface buoy hosts a vertical chain of 32 thermistors that span the thermal field in the snow/ice/water layers, and also measures air temperature, atmospheric pressure, GPS position, and the tilt of the instrument. Data are transmitted every 15 min through the Iridium communication system, the duplex mode of which enables remote adjustment of the acquisition sequence. The fish includes an upward looking sonar, a two-axis inclinometer with magnetic compass, and a pressure sensor, which are combined to provide a measurement of the ice draft. Additionally, the fish includes a Seabird SBE37 conductivity-temperature sensor, recording the temperature and salinity nominally at 6 m below the ice/ocean interface. This sensor was calibrated by the manufacturer 5 months prior to deployment, displaying residuals <0.0002°C for temperature and <0.002 mS/cm for conductivity. Finally, inclinometer/compass measurements enable estimation of the ocean currents relative to the ice, based on the principle that the fish will tilt and rise under the action of drag and lift forces (a fin orients the fish in the direction of the flow). The Ice-T buoy transmitted over 8400 data messages until DoY 191 (10 July), when it was destroyed in a compression ridge, as deduced from large tilt changes within a 2 h time frame.

2.2. POPS Buoy

A Polar Ocean Profiler System (POPS; MetOcean) was deployed by the Japan Agency for Marine Earth-Science and Technology (JAMSTEC) on DoY 102, 15 m apart from the Ice-T buoy. The POPS profiler gathered profiles of temperature and salinity between depths of 7 and 570 m with an interval of 1–2 m in depth. It is
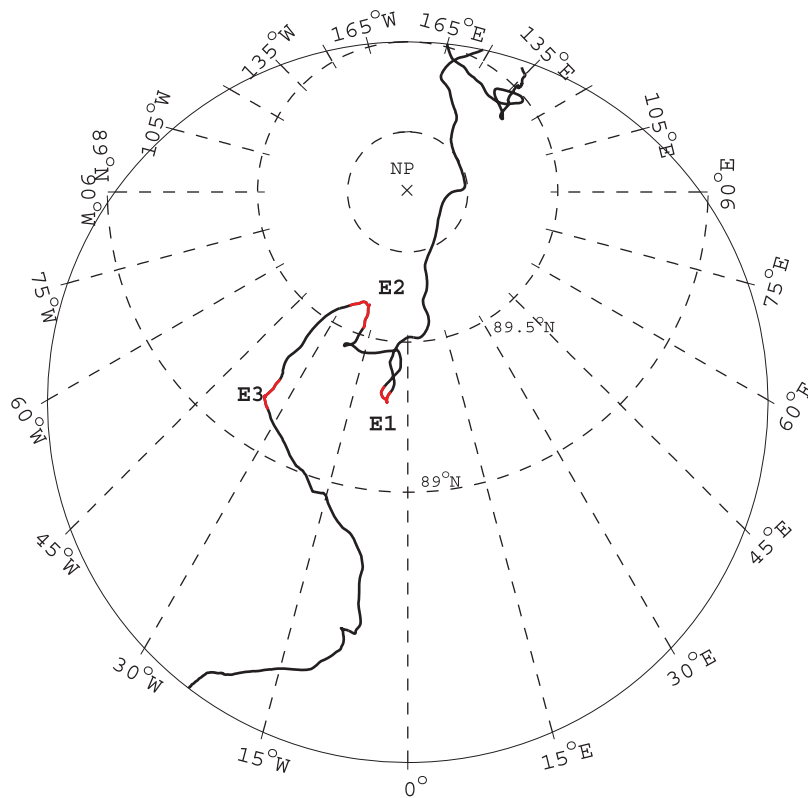
Tracking course of Ice-T/POPS

Figure 1. Track of Ice-T/POPS in 2011. Red segments denote the trajectory of the buoy array during Events 1, 2, and 3 (labeled E1, E2, and E3, respectively).

tethered to an ice-mounted surface unit that measures air temperature and pressure at 1 m height. The hydrographic sampling is performed once a day, as the instrument ascends from its parking depth. The factory acceptance test of the profiler certifies an accuracy of 0.01 and 0.001°C for salinity and temperature, respectively (for further information, see *Kikuchi et al.* [2007] and *Kawaguchi et al.* [2012]). POPS data were transmitted to the JAMSTEC office via an Iridium satellite link. However, the Iridium antenna was damaged, resulting in sporadic data transmission. Although located only 15 m away from the Ice-T, the POPS buoy was not harmed by the pressure ridge on DoY 191 and transmitted until DoY 239.
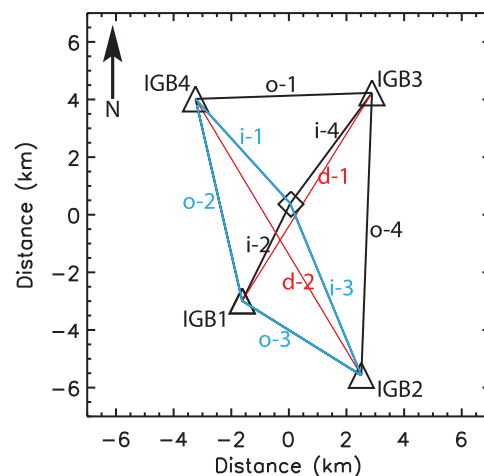

Figure 2. Schematic plot of the buoy array. The diamond at the center denotes the POPS/Ice-T position. Two sets of buoy combinations, (IGB-1, IGB-2, IGB-3, and IGB-4) and (POPS/Ice-T, IGB-1, IGB-2, and IGB-4), are used to calculate ice area change. The second, smaller array is outlined in cyan. Segments labeled o, i, and d denote outer, inner, and diagonal lines of the array, respectively.

2.3. GPS Buoys and Webcam

The Ice-T and POPS buoys were collocated with a web camera installed by the Polar Science Center (Applied Physics Laboratory, Seattle), which transmitted photographs up to 4 times a day (http://www.arctic.noaa. gov/gallery np.html). Four GPS ice drifters from the International Arctic Research Center (IARC, University of Alaska, Fairbanks), placed approximately 5 km to the northwest, northeast, southeast, and southwest of the POPS/Ice-T site completed the experimental setup (Figure 2). Hereinafter, these GPS drifters are referred to as IARC GPS buoy (IGB) with buoy identification
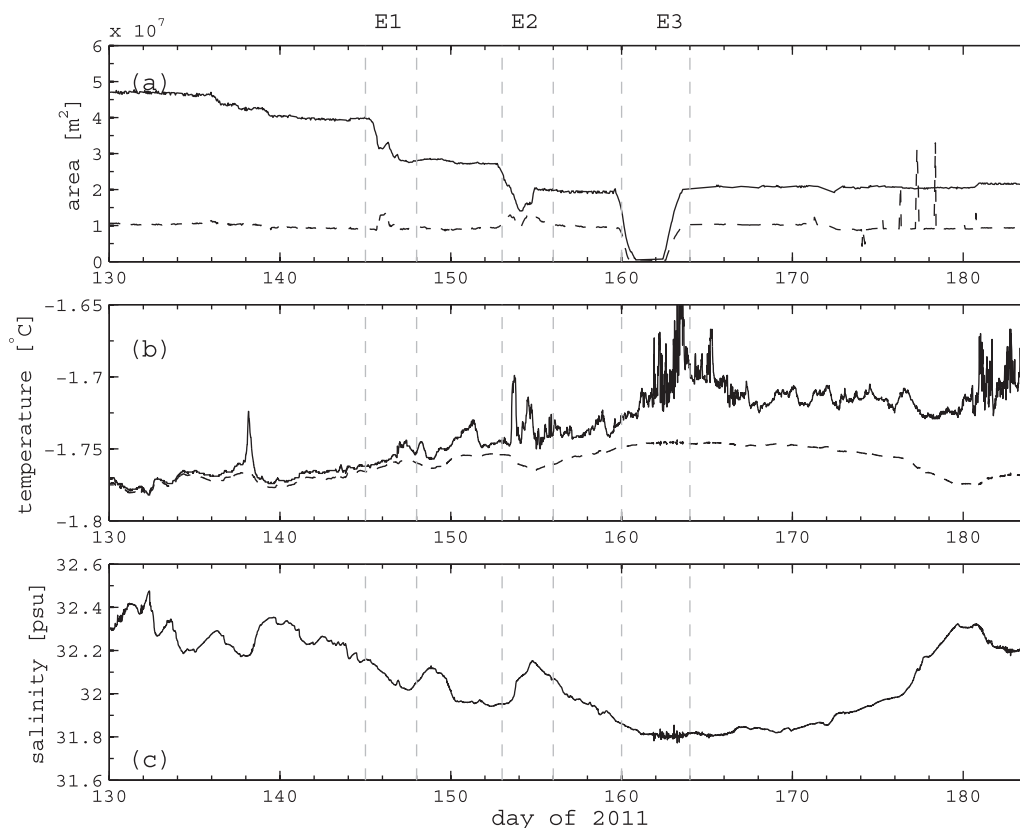
Figure 3. Time series of (a) buoy array area, (b) temperature, and (c) salinity measured by the Ice-T 6 m below the ice base. In Figure 3a, the area plotted as a solid line is an estimate based on the positions of four GPS drifters (IGB-1, IGB-2, IGB-3, and IGB-4), while the dashed curve is based on the position of Ice-T/POPS and three drifters (IGB-1, IGB-2, and IGB-4). Please refer to Figure 2 for the configuration of the two buoy arrays. In Figure 3b, the dashed curve denotes freezing temperature. Vertical lines in each figure denote times at which deformation events happened.

numbers 1–4 (Figure 2). The IGBs provided 10 min positions from which ice velocity and strain-rate components (shear, divergence, and vorticity) were estimated as per *Hutchings et al.* [2012]. The Ice-T and IGBs formed an array that was split into smaller subarrays, for which area and strain-rate components were computed hourly. We consider the subarrays (shown in Figure 2) which provide the best representation of lead opening and ridging in the vicinity of the Ice-T and POPS buoys. Note that IGB-1 stopped data transmission mid-July when it was likely destroyed during pressure ridge formation.

3. Analysis of Drifting Buoy Data

3.1. Trajectory and Deformation of the Buoy Array

The buoy array was deployed to the west of the Lomonosov Ridge on DoY 102 (Figure 1). It initially migrated eastward before following a meridional trajectory toward and then away from the North Pole in a southward course following the Trans Polar Drift Stream (TPDS). The array traveled a distance of ∼620 km between DoY 102 and DoY 191, when the Ice-T transmission stopped. The average speed of the buoy array was 8.1 cm s^{-1} (7 km d^{-1}).

Between DoY 144 and 166 (24 May and 15 June), three distinct ridging events, which were followed by openings, were detected in the buoy array deformation (Event 1 from DoY 144 to 147, Event 2 from DoY 152 to 155, and Event 3 from DoY 159 to 164). Figure 3 shows that a sharp decrease in the IGB array area occurred during each ridging event. These transformed the shape of the buoy array through shear and convergence over periods of less than 4 days, as displayed in Figure 4.

During Event 1, the entire buoy array moved to the north, against the mean TPDS direction (Figure 1). IGB-4 moved rapidly to the southwest relative to center of the array (Figure 4), so that segments $o-1$ and $i-1$
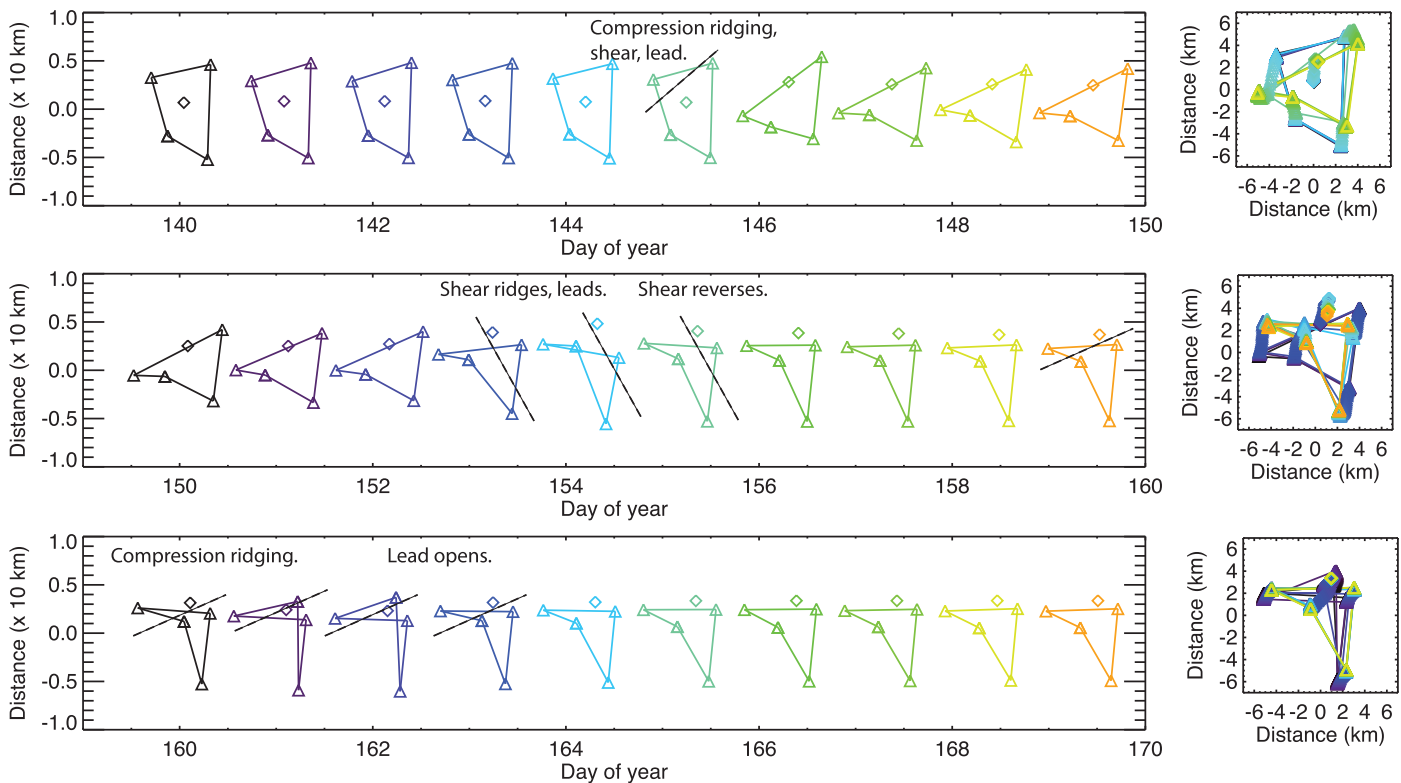
Figure 4. Evolution of buoy array shape during three ridging events: (top) Event 1, (middle) Event 2, and (bottom) Event 3. Diamonds and triangles denote positions of the POPS/Ice-T and GPS drifters, respectively. Colors denote the time evolution of the array transformation, from cold to warm colors. The boxes in the right overplot the changing array shapes during each event.

(Figure 5) lengthened significantly, through shearing along a lead (Figure 4), creating nearly 5 km of open water along the segment. The lead was orientated southwest to northeast, and remained open through DoY 155 (the end date of Event 2). The Ice-T and POPS buoys shifted to the north of the array center during Event 1.

During Event 2, the POPS/Ice-T moved farther north, drifting apart from the other buoys by more than 3 km, before reversing to the south, moving ∼2 km southward by DoY 157 (Figure 4). During this event, the array sheared into two pieces. Segments $i-3$ and $o-3$ showed a marked elongation (Figure 5), perpendicular to which a lead formed with roughly north-south orientation. During this period, large ridging and lead opening events were captured by the web camera (Figure 6). Photographs show that the lead initially opened on DoY 150, and continued to open and close with ridging twice in 5 days. On DoY 154, the entire buoy array was sheared, splitting the camera buoy from the Ice-T/POPS buoys.

During Event 3, between DoY 159 and 164, the buoy array experienced the greatest magnitude of shear and compressive deformation (Figure 4), while all of the buoys were nearly stationary at (89.2°N, 33°W) for almost 1 week (Figure 1). Between DoY 159 and 163, IGB-1 that was initially deployed to the southwest of the POPS/Ice-T buoys migrated northward toward POPS/Ice-T and moved temporarily out of the triangle formed by the other GPS buoys. The distance between this buoy and the POPS/Ice-T position reduced on DoY 162. IGB-1 then nearly returned to its original relative position in 1 day. Judging from the temporal evolution of segment lengths $o-2$, $o-3$, and $i-2$ (Figure 5), we infer that large ridges formed through compressive motion between DoY 159 and 162, whereas after that, a reversed motion led to the opening of an east-west directed lead.

3.2. Surface Water Warming Concurrent With Ice Deformation Events

Prior to the ridging events, the ocean temperature 6 m below the ice at the Ice-T followed the freezing point (Figure 3). There was one peak in temperature in mid-May on DoY 139. This perturbation in temperature nearly coincides with a small deformation event happening on DoY 138–139, but in situ temperature
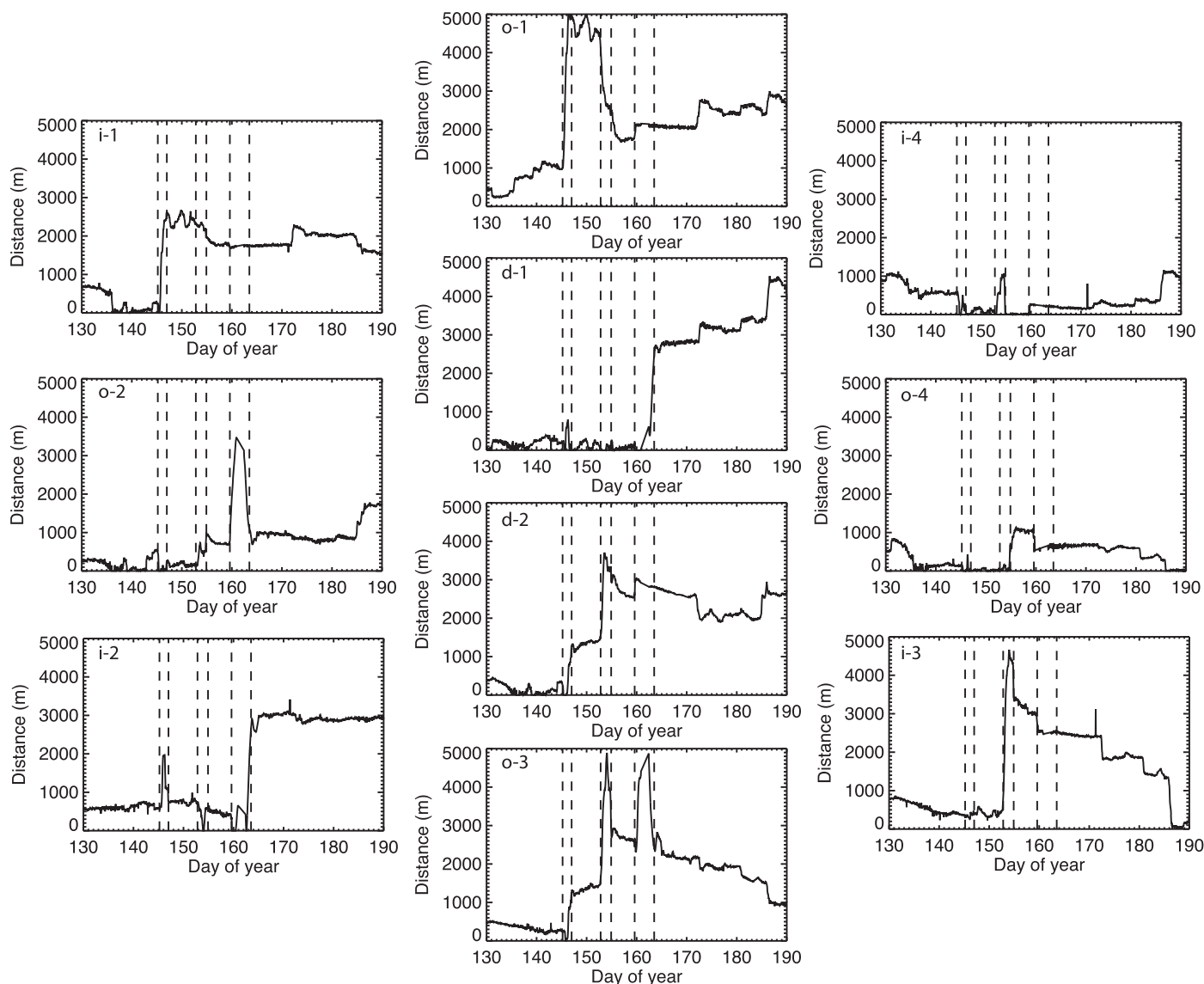
Figure 5. Temporal evolution of line lengths between buoy pairs, which are subtracted from the initial lengths. Each segment corresponds to those marked on the schematic plot of Figure 2. Dashed lines denote timing at which each event happened.

quickly returned close to the freezing point. During the second and third ridging events, the Ice-T sensor recorded more significant temperature deviations from the freezing point. The timing of these peaks coincides with opening of leads after ridging, suggesting that heating may be provided by solar absorption while the leads remained open and unfrozen (the issue of heat source will be discussed later). Continuous departure from the freezing temperature at 6 m below the ice occurred around DoY 148, which was the day after the start of Event 1. From the buoy array deformation, we see that Event 1 was the largest opening event after array deployment. This event marked the start of the transition between a winter and summer mixed layer (ML), as the temperature rose above the freezing point.

From webcam photographs, we have visual evidence that a lead opened in the vicinity of the Ice-T during Events 2 and 3. These coincide with an elevation of the ML temperature. During Event 3, the Ice-T recorded the highest water temperature at 6 m below the ice of the entire observation period exceeding the freezing point by more than 1°C (Figure 3b), hinting at an input of heat by solar radiation through open leads. We further address in the following sections how temperature and salinity profiles evolved during these events, and whether documented lead openings were merely local or consistent with dynamics at larger scales.
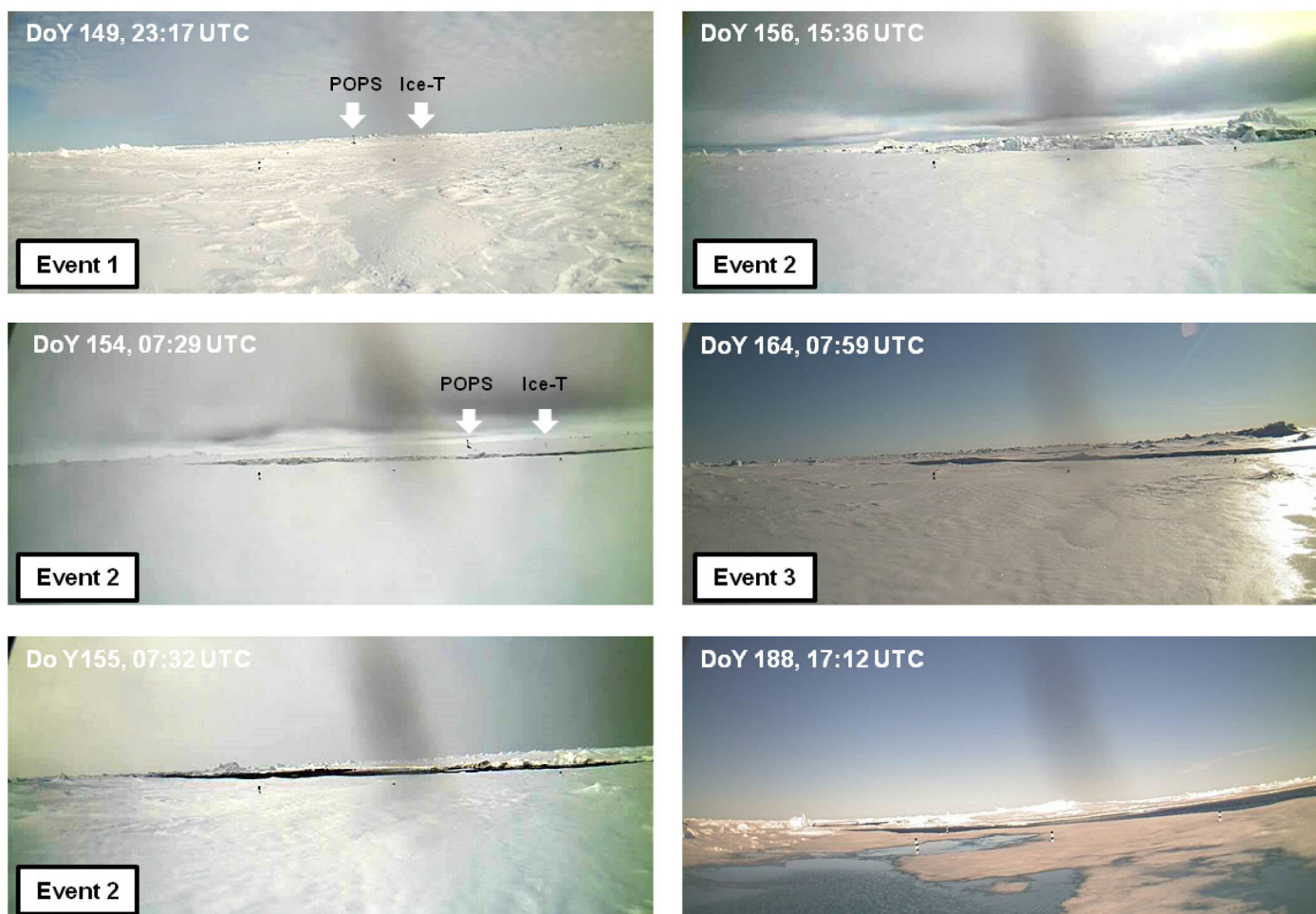
Figure 6. Selected photographs taken by web camera. POPS and Ice-T are in sight of the webcam view until DoY 154 of Event 2. A lead, which was formed in early Event 2, sheared Ice-T/POPS from the ice floe on which the webcam was installed. Melt ponds started to form after Event 3.

Salinity decreased by ∼0.4 (from ∼32.2 to 31.8) during the period spanning the three events (Figure 3c). While one would expect a freshening of the water below the ice associated with ice melt, we will show below that the freshening rate of the ML cannot be accounted for by melting alone during this short period, suggesting that horizontal advection (or equivalently displacement of the buoy array through fresher water masses) is an important component of the salinity budget. This is consistent with the analysis of *Timmermans et al.* [2011] who showed that appreciably fresher surface water observed in 2010 (1 year before) in the Eurasian Basin was likely due to a spreading of anomalously freshwater from the Beaufort Gyre.

3.3. Mixed Layer
Although sporadic data transmission did not provide high fidelity data, the POPS buoy was able to track changes in the mixed-layer depth during the drift (filled circles in Figure 7), defined as the depth where the squared Brunt-Väisälä frequency N^2 is maximum in the first 100 m. Depths where N^2 exceeds 1.0×10^{-4} s^{-2} are also indicated (crosses in Figure 7). The winter mixed-layer (WML) depth remained stable around 40–50 m during the three events between DoY 140 and 170. A localized deepening of the WML occurred around DoY 125, suggesting that the buoys intercepted oceanographic structures like mesoscale eddies or fronts.

Figure 7 reveals that during the first two events, the upper ocean (below 7m) is well mixed, with nearly homogeneous salinity and temperature. By contrast, during Event 3 (DoY 159–164), there is indication of a shallow warming within the WML, where temperature is greater by 0.05–0.07 K than that during Event 2. This warming rapidly decays with depth, with nearly zero deviation from freezing point below 20 m.
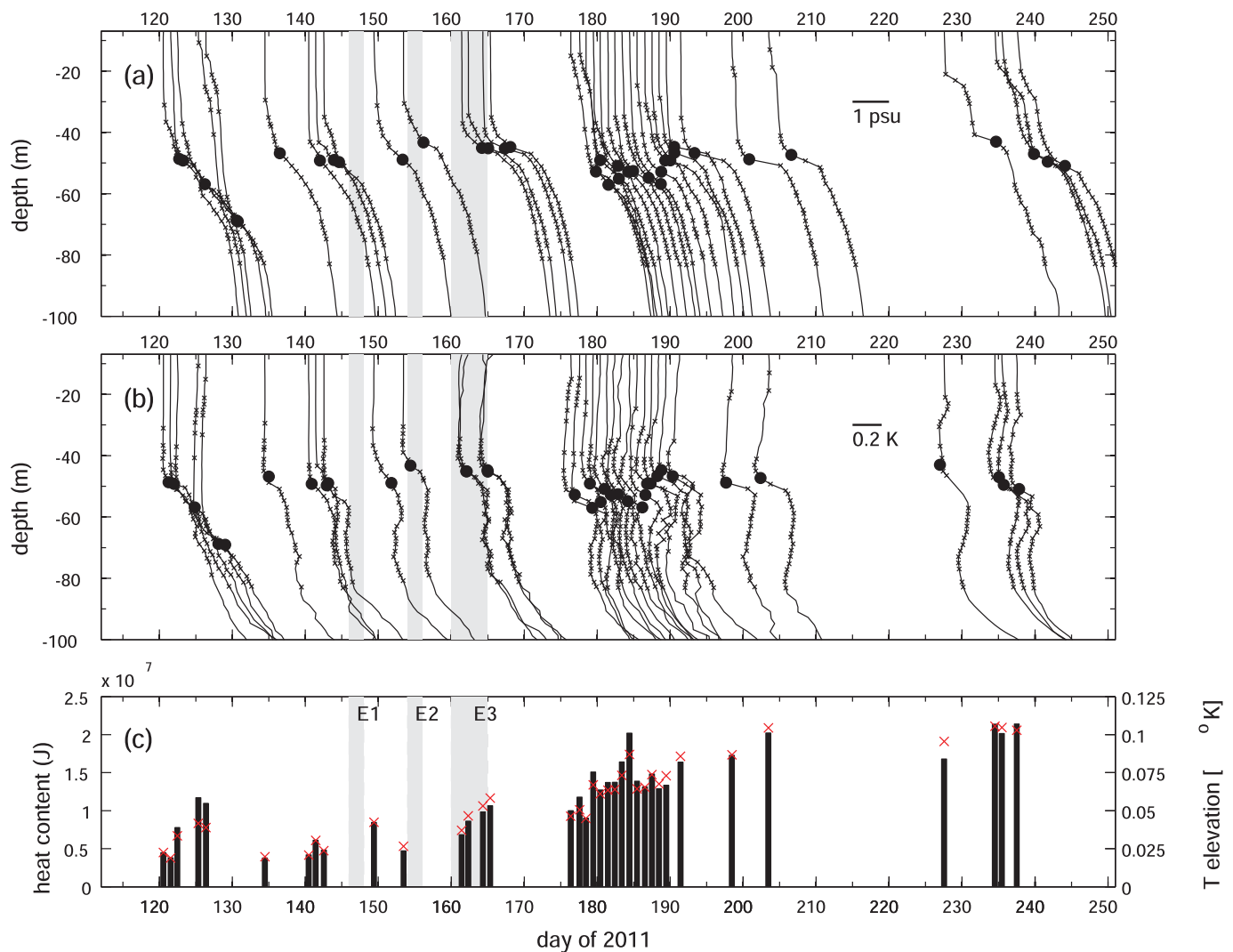
Figure 7. Time series of (a) salinity, (b) potential temperature profiles, and (c) heat content in the mixed layer from POPS observations. On the profiles, filled circles denote the maximum stratification within 100 m in depth, and crosses denote depths with squared Brunt-Väisälä frequency N^2 greater than 1.0×10^{-4} s^{-2}. Figure 7c also displays temperature deviations from the freezing point at zero pressure, averaged over the mixed-layer depth (red crosses, right scale).

Regarding salinity, there does not seem to be any notable vertical structure throughout the WML. These observations are suggestive of a solar warming of the upper ocean during Event 3.

A secondary N^2 maximum developed at 20–30 m, first sporadically around DoY 177, and then persistently after DoY 195. It is presumably due to an accumulation of freshwater associated with sea ice melt. We distinguish this shallow layer, referred to as surface summer layer (SSL), from the deeper and stable WML.

The heat content of the mixed layer is estimated by integrating the temperature measured by the POPS buoy between 7 m and the WML depth (Figure 7). It was comparatively low during the first two ridging events, with respect to the full period over which POPS worked (DoY 102–239; 12 April to 27 August). The mixed-layer heat storage picked up during Event 3 and subsequently further increased between DoY 175 and 185, consistently with Ice-T data (Figure 3b). Temporal variation of the mean temperature of the WML was generally in accordance with the heat storage integrated within the layer (Figure 7c).

3.4. Evolution of Ice Thickness

The determination of ice thickness from Ice-T involves several processing steps. The distance between the fish and the ice base is determined from sonar measurements after correction for the fish
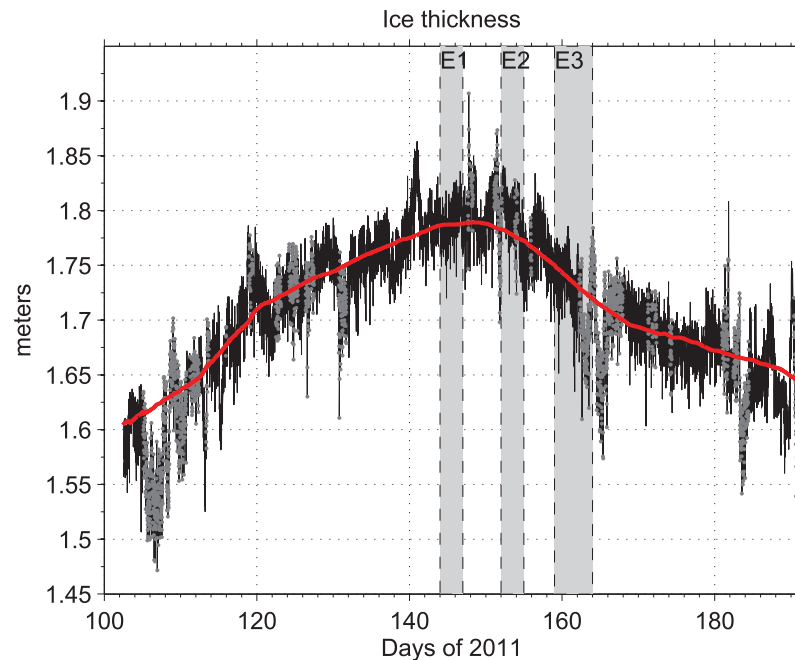
Figure 8. Evolution of ice thickness as estimated by the Ice-T. Black line denotes the raw estimate, while the red line shows low-pass filtered ice thickness with a cutoff period of 20 days. Gray dots mark estimates with larger uncertainty (see full description in section 3.4).

inclination with respect to the vertical. The depth of the fish is determined from underwater pressure measurements corrected for atmospheric pressure variations. These measurements all together provide an estimate of the ice draft. However, because the fish is not rigidly attached to the surface buoy and is free to move under the action of the ice-ocean relative currents, it may not always insonify the same part of the ice floe. Rather, inclination/depth data indicate that the sonar illuminates different regions located on a 2 m radius circle with the surface buoy at the center. This is inconsequential if the floe is perfectly flat, but this was not the case here. The bottom topography of the floe was mapped with a series of drill hole measurements, which indicate bottom relief of about ∼10 cm over a 4 m horizontal scale. This can in principle be corrected by tracking the rotation of the fish, but the compass used in 2011 turned out to lack the required sensitivity near the North Pole where the horizontal component of the Earth magnetic field is small. We used instead heading information derived from the buoy's GPS fixes, assuming that the ice drift speed exceeds ocean currents. When the drift velocity is too small (<5 cm s^{-1}), we consider that heading from GPS cannot deliver an accurate orientation of the fish anymore and data are flagged as inaccurate. Once the ice draft is determined, the ice thickness is derived using information on seawater density (continuously measured), ice density, and snow load (both measured at the time of deployment). The high-frequency noise in the ice thickness measurements is 3 cm RMS (Figure 8), reduced to 2.4 cm RMS if we exclude data where the rotation correction could not be applied. Because of the high sampling rate (96 measurements per day), applying a low-pass filter with a cutoff period of 20 days on these estimates provides accurate time series of ice thickness, which are considered hereinafter.

Figure 8 shows that ice thickness at the Ice-T/POPS site increased by ∼20 cm in 45 days through bottom accretion until about DoY 146. It then remained approximately constant before starting to decrease around DoY 148. This timing matches the moment when the temperature at 6 m below the ice starts departing from the freezing point (Figure 3b). The decrease in thickness is relatively fast between DoY 150 and 165, coincident with Events 2 and 3, during which thickness reduced by ∼7 cm over 2 weeks. Photographs from the web camera indicate that the onset of surface melt occurred on DoY 166, and melt ponding commenced on DoY 181 (Figure 6). The timing of surface melt is confirmed by thermistor measurements from the Ice-T in the snow, which abruptly reach 0°C on DoY 169 (not shown). Our observations therefore indicate that the onset of basal melt preceded surface melt by ∼20 days.
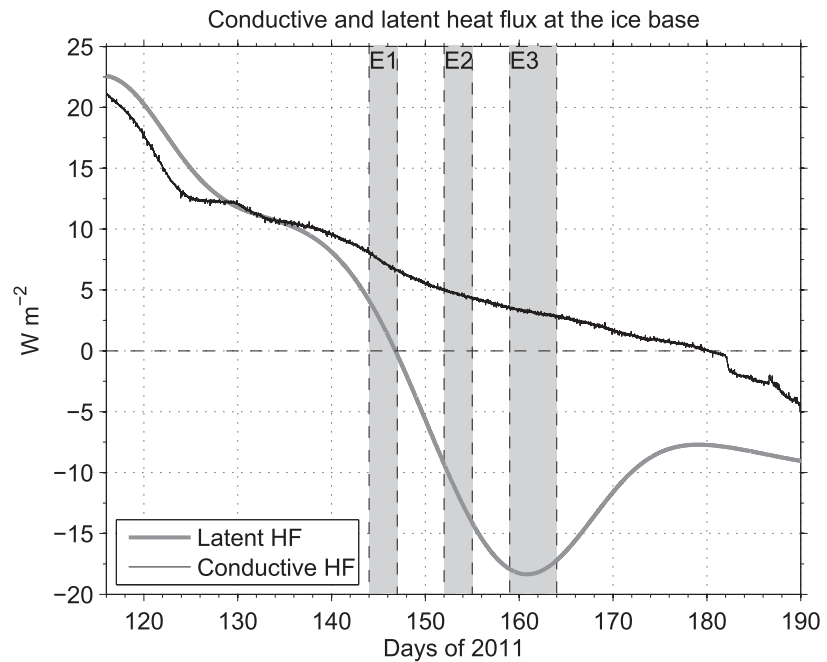
Figure 9. Conductive heat flux within the ice (black solid line) and latent heat flux at the base of the ice (gray line) derived from Ice-T data. The conductive heat flux is calculated from ice interior temperature gradient at 10 cm above the ice bottom. Flux is positive upward.

3.5. Conductive Heat Flux in the Ice and Latent Heat of Fusion

The conductive heat flux through the ice, $\dot{q}$, is estimated from the temperature gradient within the ice according to

$$\dot{q} = -K_{ice}\frac{\partial T_i}{\partial z}. \tag{1}$$

The thermal conductivity of sea ice, K_{ice}, is derived from the formulation of Pringle et al. [2007]: $K_{ice} = \rho_i/\rho_{pi}\left(2.11 - 0.011 T_i + 0.09\, S_i/T_i - (\rho_i - \rho_{pi})/1000\right)$, where ρ_{pi} is the density of pure ice (917 kg m^{-3}) and ρ_i, T_i, and S_i are the bulk density, temperature, and salinity of sea ice, respectively. We take $S_i = 5$ and $\rho_i = 935$ kg m^{-3}, according to measurements from ice cores during deployment, while T_i is obtained from the Ice-T's lateral thermistors chain. The vertical gradient of ice temperature is estimated from the pair of thermistors closest to the ice bottom as tracked by acoustic measurements. Note that only temperature data later than DoY 115 are considered in this calculation, to ensure that the hole drilled for deployment has refrozen over its full depth. The spacing between thermistors near the ice bottom was 12.5 cm (the spacing was refined to 2 cm near the snow/ice interface).

The latent heat flux at the ice base, H_f, is computed from the 20 day low-passed ice thickness, h_{ice}, according to $H_f = \rho_{pi}L\frac{\partial h_{ice}}{\partial t}$, where $L = 333.4$ kJ kg^{-1}.

Conductive and latent heat fluxes are shown in Figure 9. $\dot{q}$ sharply decreased from 21 to 12 W m^{-2} between DoY 115 and DoY 125, and subsequently showed a smaller decreasing trend. The latent heat of ice growth, H_f, prior to the onset of basal melt was mostly provided by the conductive heat flux: before DoY 146, the conductive heat flux matched the latent heat flux to within less than 3 W m^{-2}. At this time, ice thickened by 12 cm in 30 days (Figure 8), corresponding to an average latent heat flux of 14 W m^{-2}, consistent with the conductive heat flux displayed in Figure 9, ranging between 21 and 7 W m^{-2} during this period. This two term heat balance at the ice-ocean interface is further confirmed by the fact that oceanic turbulence supplied almost no heat before DoY 146, since the mixed-layer temperature virtually remains at the fusion point (Figure 3b).

The conductive heat flux remained positive even after the onset of basal melt, decreasing until DoY 182, where it switched to negative values after sufficient warming of the ice interior (a flushing of the brine network from melt ponds may have contributed to raise the fusion point). During this period, encompassing in

particular the three events, the conductive heat flux averaged to 2.9 W m^{-2} (Figure 9), so that in the absence of additional heat source at the ice bottom interface, basal ice growth would be expected. Instead, the ice melted by ∼12 cm in 34 days, corresponding to an average latent heat flux of ∼−11.8 W m^{-2}.

4. Heat and Salt Budget of the Mixed Layer

4.1. Missing Heat Flux

Examination of the thermodynamical sea ice mass balance from the previous section indicates that an additional average ocean-ice heat flux of 14.7 W m^{-2} (imbalance between conductive and latent heat fluxes) is required to explain the observed melting rate after DoY146.

We also recall from section 3.3 that the ML started to warm during this period. Prior to Event 1, the temperature elevation was close to the freezing point. It increased by ∼0.04°C by DoY 182. If we assume a well-mixed WML, we can estimate the heat storage as $c_P h_w \rho_w \Delta T / \Delta t$, where $c_P = 4008$ J kg^{-1} and $\rho_w = 1026$ kg m^{-3} are the specific heat and density of seawater, respectively, and h_w is the mixed-layer depth estimated to be 45 m from POPS data, and ΔT is the change in temperature during the period Δt. A constant heat flux of about 2.5 W m^{-2} is required to explain the observed temperature increase during this period. The hypothesis of a permanently well-mixed WML is disputable as POPS observations suggest a temperature rise enhanced in the upper 20 m during Event 3. This estimate of the heat storage should therefore be taken as an upper bound.

To identify where the additional ∼17.2 W m^{-2} heat flux needed to melt the ice (14.7 W m^{-2}) and warm the WML (2.5 W m^{-2}) originates, we consider the energy budget over a column of upper ocean. The ocean column heat storage is balanced by the ocean-ice heat flux, and heat input to the column from the sides (lateral mixing with water warmed in leads) and below. At leads incoming solar radiation is balanced by change in heat storage in the water and longwave, sensible and latent heat losses at the surface.

4.2. Vertical Advection

We have considered warm water upwelling associated with shearing ice motion as a possible heat source. *McPhee et al.* [2005] report that shearing ice motion across an active ridge produced a notable upwelling event, followed by a significant warming in the upper water. Our calculation [following *McPhee et al.*, 2005] based on our observed shearing buoy motion [as *Hutchings et al.*, 2012] indicates that the WML depth would change by less than 3 m during the deformation events. The warm Atlantic water, underlying the WML, needs to be lifted by more than 40 m to contribute to the basal ice melt. Hence, the upwelling of the underlying pycnocline water is unlikely to be the main source of heat for the basal ice melt in the present case. This conclusion is consistent with our observation of an approximately constant WML depth from POPS data, despite the gaps in the series.

4.3. Surface Warming at Leads

To examine the energy input at leads, we estimate lead fraction from the daily sea ice concentration (SIC) maps at a 6.25 km resolution derived from AMSR-E microwave radiometer data based on the Artist Sea Ice (ASI) algorithm using the 89 GHz channel temperature [*Spreen et al.*, 2008]. Because of the orbit of the Aqua satellite that hosts AMSR-E (98.2° inclination), no data are available north of 89°N. A time series of daily sea ice concentration was nevertheless constructed by averaging AMSR-E maps in the region encompassing the buoys' trajectory after they passed the North Pole, that is between 320°E and 15°E and north of 88°N. An alternative time series was obtained by interpolating at the buoys location the sea ice concentration from the ERA-interim (ERAI) global reanalysis from the European Centre for Medium-Range Weather Forecasts (ECMWF) available every 6 h at a 0.75° resolution, subsequently averaged on a daily basis. These estimates are shown in Figure 10a, displaying rather consistent variations. It is noteworthy from this figure that the three events identified from the buoy array are almost coincident with three significant drops both in AMSR-E and ERAI sea ice concentration time series (particularly large for Event 3), suggesting that locally observed lead openings were part of a larger-scale pattern. On the other hand, both series indicate substantial reduction in SIC from 1 to 0.85 around day 125, which is not reflected in our local observations.

Perovich [2005] identified that in Spring over 90% of incident solar energy over open water is absorbed in the ocean, and solar transmission through snow and ice is minimal. Using downward shortwave radiation from ERAI, F_r, we can determine the available shortwave radiation for the mixed layer as
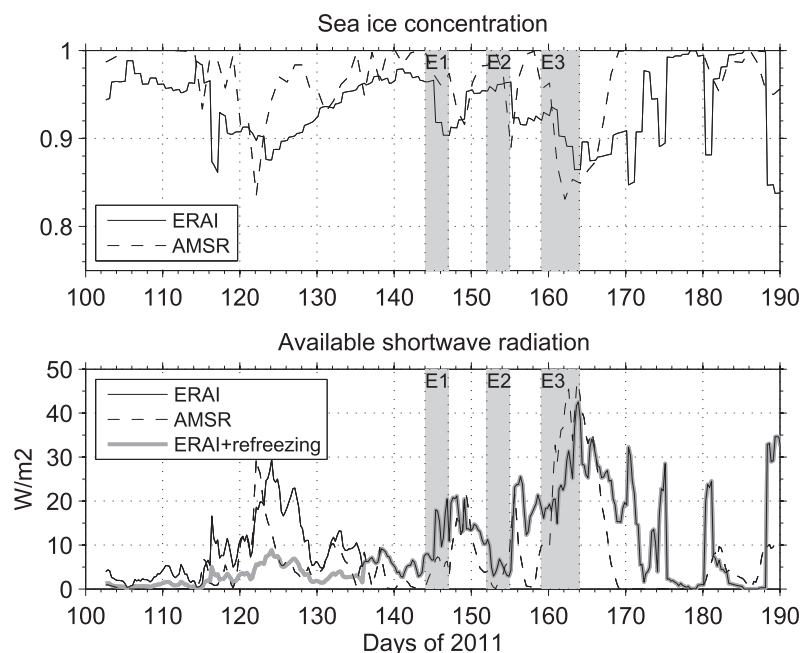
Figure 10. (top) Sea ice concentration and (bottom) shortwave radiation available for the mixed layer. The sea ice concentration is obtained from ERA-interim (dashed) and AMSR-E satellite data (solid). The available shortwave radiation is computed from ERA interim's downward shortwave radiation, accounting for the open water fraction estimated from AMSR-E (dashed) or ERA interim (solid), using an albedo of 0.11 for open water. The gray bold line indicates the available shortwave radiation based on ERA-interim sea ice concentration, but further assuming that leads refreeze prior to day 135 (see text).

$F_i = (1 - SIC)(1 - a)F_r$, where a is the albedo of open water [e.g., *Perovich et al.*, 2008; *Toole et al.*, 2010; *Stanton et al.*, 2012]. In these studies, the albedo of open water is taken as 0.07. We expect a somewhat larger value near the North Pole, as albedo significantly depends on the solar elevation angle, approximately following the Fresnel equation [e.g., *Cogley*, 1979]. During the period of interest (DoY 140–190), the solar elevation was fairly constant, ranging between ∼20° and ∼24° (it was in particular independent of the hour at this latitude). For such elevations, an albedo of ∼0.15 is expected [*Cogley*, 1979; *Jin et al.* 2004]. The roughness of the sea surface associated with winds tends to attenuate the reflectivity at high latitude, however, contributing to lower the albedo. This effect has been parameterized by *Pegau and Paulson* [2001], who provide a polynomial expression depending both on the solar zenith angle and wind speed. At wind speeds of 20 m s^{-1}, albedo can decrease down to 0.09. We take an average value of 0.11 for subsequent analyses.

The available shortwave energy is shown in Figure 10b. Between DoY 146 and 182, it averages to 10.6 W m^{-2} using SIC from AMSR-E and to 15.8 W m^{-2} using SIC from ERAI, which is comparable to the 17 W m^{-2} we are looking for.

This simple budget is based on the hypothesis that leads do not refreeze after DoY 146, as even a thin layer of reforming ice would greatly reduce the fraction of incoming solar radiation available for the mixed layer. This hypothesis was examined by estimating the turbulent and net longwave heat flux at the lead surface.

Turbulent sensible and latent heat fluxes were computed from bulk formulae based on the parameterization of *Fairall et al.* [1996], using atmospheric pressure, 2 m air temperature, relative humidity, and 10 m wind speed from ERAI, while the sea surface water temperature was assumed to be at −1.7°C. Note that air temperature and atmospheric pressure data from ERAI closely match observations from Ice-T or POPS (not shown). This agreement is not surprising since data from weather buoys deployed as part of the NPEO were distributed through the Global Telecommunication System (GTS), and were therefore assimilated in atmospheric reanalyses used here.

The net longwave heat flux was computed also from a bulk formula using the formulation of Berliand [see *Fung et al.*, 1984] using air temperature, relative humidity, and total cloud cover information from ERAI, while still assuming a sea surface temperature of −1.7°C.
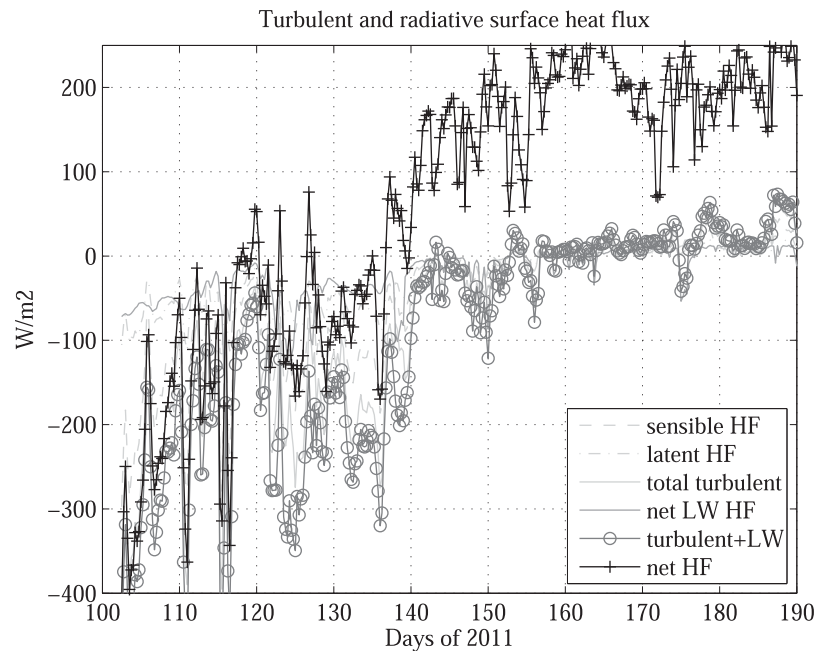
Figure 11. Turbulent and radiative heat fluxes assuming open water at −1.7°C. The net longwave radiative heat flux as well as the sensible and latent turbulent heat fluxes are computed from bulk formulae. Their sum is denoted by circles. The total heat flux (plus) includes short-wave radiation from ERA-interim. Negative values indicate a heat loss from the ocean.

Turbulent and net longwave fluxes are displayed in Figure 11. Both latent and sensible turbulent fluxes were negative until DoY 136, where they reached a value close to zero, due to the sharp rise in air temperature. The net longwave radiative heat flux exhibits a similar behavior, turning from large negative values to values close to zero on DoY 136. The sum of the turbulent and longwave radiative fluxes (circled line in Figure 11) likewise shows a marked transition around DoY 136, where it turns from large negative values (up to -300 W m^{-2}) to zero and then slightly positive values. The large negative net heat flux prior to DoY 136 can be translated in terms of rate of ice formation: these correspond to the formation of 5–10 cm of ice per day, indicating that leads quickly refreeze before DoY 136. This greatly affects light transmission to the ML, since the albedo of bare ice is $\sim$0.63 [*Perovich et al.*, 2002], while light is further absorbed through the ice following a Beer-Lambert law with an extinction coefficient of 1.5 m^{-1} [e.g., *Maykut and Untersteiner*, 1971]. The effect of a refrozen lead with a thickness of 10 cm on light transmission prior to DoY 136 is displayed in Figure 10b, showing that the available shortwave energy is reduced by about two third. The impact of the large lead opening around DoY 125 on the heat budget is thus limited.

This analysis suggests that we can model the evolution of the ice thickness and ML temperature considering solely the input from the shortwave radiation after DoY 136. Indeed Figure 11 additionally shows that the sum of the net turbulent and longwave fluxes is more than 1 order of magnitude smaller than the shortwave radiation after this date and can thus reasonably be ignored. The same assumption is made in several previous studies focusing on summertime [e.g., *Perovich et al.*, 2008]. In section 5, we investigate how solar energy input through leads influences the structure of the upper ocean. A 1-D model is used to understand mechanisms controlling how solar input is partitioned between ocean warming and ice melt.

4.4. Salinity Budget
Figure 3c indicates a continuous decrease in salinity from DoY 143–170 from 32.2 to 31.8. During this period, ice thickness decreased by $\sim$10 cm (Figure 8). The expected drop in salinity assuming meltwater is fully mixed through the ocean's ML depth, is

$$\Delta S = S_{w0} - \frac{\rho_w h_w S_{w0} + \rho_i dh_i S_i}{\rho_w h_w + \rho_i dh_i}, \qquad (2)$$

where dh_i is the thickness of melted ice, and S_{w0} is the initial salinity of seawater (32.2). With $h_w = 45$ m, this equation yields $\Delta S = 0.05$, far from the observed drop of 0.4. In fact it would require mixing over a depth of 6 m to get such a drop in salinity, which is contradicted by POPS observations. Even assuming that 30 cm of snow has melted (an assumption contradicted by webcam observations), we would merely get a total salinity drop of 0.12. We conclude that the change in salinity is for the most part owed to horizontal advection (or equivalently displacement of the buoys into fresher water masses).

The importance of lateral advection may preclude a simple 1-D heat budget approach. Figure 3c shows that largest salinity changes occurred somewhat gradually before day 155. Up to that date, the temperature was still close to the freezing point (Figure 3b). Advection into a water mass that is 0.3 fresher results in an elevation of the freezing point of 0.02°C. The largest deviation of the in situ temperature from the freezing point occurs during Event 3, after DoY 160, when salinity remains approximately constant for about 10 days. It therefore seems consistent to hypothesize that temperature changes are for the most part owed to solar warming through leads, at least for this part of the record. It is for this reason we proceed with a one-dimensional simulation to investigate the heat budget in the upper ocean.

5. One-Dimensional Mixed-Layer Simulation

To guide interpretation of the evolution of the upper-ocean structure, heat content, and ice thickness, we consider how oceanic properties such as heat, salinity, and momentum are redistributed in the upper ocean using a one-dimensional (1-D) numerical model. Unlike *Toole et al.* [2010] who coupled two 1-D mixed-layer models for summer simulations, one with open water mimicking open leads and one covered by ice, based on the Price-Weller-Pinkel algorithm (PWP) [*Price et al.*, 1986], we use the Local Turbulence Closure (LTC) model [*McPhee*, 1999, 2008]. This takes into account the thermodynamic ice-ocean interaction, and in particular, the penetration of solar radiation, although in our application solar radiation will have the magnitude expected from a penetration directly into the open ocean rather than through the ice. We realize that such a 1-D model will not be able to account for salinity changes due to advection. From the previous section, we suspect lateral advection of freshwater occurred, and temperature changes associated with the corresponding displacement of the freezing point will not be reproduced in the 1-D model. *McPhee* [2008, chapter 8] recognizes that "often relatively small horizontal gradients encountered as the ice drifts will swamp the signal from local vertical exchanges." He additionally implements a correction by specifying a constant advective source term based on observed salinity. As salinity changes differ from a constant drift in our series, and as we lack regular observed salinity profiles through the mixed layer, such a correction was not attempted here.

5.1. Model Configuration
5.1.1. Main Model
We have performed simulations of the ice-ocean boundary layer for the period between DoY 134 and 183, thus starting approximately when the net surface heat flux becomes positive at leads, encompassing the dates of Events 1, 2, and 3, and ending with the conductive heat flux becoming positive at the base of the ice. Our aim is to identify how solar heat input controls the evolution of the mixed layer, how the heat can be redistributed in the layer, and how large an amount of surface heat input is used in basal ice melt. Consistent with the analysis of section 4, we hypothesize that all added heat originates from the incident solar radiation in leads resulting from ice deformation [e.g., *Perovich et al.*, 2008]. For the initial conditions, we use temperature and salinity profiles obtained by the POPS on DoY 134. The model uses a uniform grid cell spacing of 20 cm. For the upper boundary conditions, fluxes of salt, heat, and momentum are computed within a submodel of the ice/ocean interface (described further below) forced by the conductive heat flux in the ice and the friction velocity derived from the observed ice drift or winds depending on experiments. At the lower boundary, 100 m, zero stress is assumed.

The model solves 1-D conservation equations for temperature, salinity, and momentum under vertical diffusion. The model incorporates a Local Turbulence Closure scheme [*McPhee*, 1999] for determining vertical eddy diffusivity of heat, salt, and momentum (K_h, K_s, and K_m, respectively). The eddy viscosity $K_m(z)$ is determined as a product of the friction velocity in the water interior, u_*, and the mixing length scale, λ, that is the scale of under-ice eddies that provide the bulk of the momentum transfer. The core of the LTC lies in

the determination of the scale λ, which grows with distance from the interface until reaching a limiting size λ_{max}, determined by the interplay between shear stress and buoyancy flux at the interface [*McPhee*, 2008].

In the neutral or stable case (e.g., melting), λ grows linearly with distance according to $\lambda = \kappa|z|$ for $\lambda < \lambda_{max}$, otherwise it is set to be $\lambda = \lambda_{max}$, where $\lambda_{max} = \eta_*^2 \Lambda_* u_{*0}/|f|$ and $\eta_*^2 = \left(1 + \frac{\Lambda_* \langle w'b' \rangle_0}{R_c|f|u_{*0}^2}\right)^{1/2}$ with constants of $\kappa = 0.4$ (von Kármán's constant), $\Lambda_* = 0.028$ (similarity parameter), and $R_c = 0.2$ (critical flux Richardson number). The buoyancy flux $\langle w'b' \rangle_0$ is provided by the submodel at the ice/ocean interface (see below).

In the unstable case (freezing), the mixing length scale grows according to $\lambda = \kappa|z|\left(1 - \frac{|z|}{L_O}\right)^2$ for $\lambda < \lambda_{max}$, and set to λ_{max} beyond. L_O is the Obukhov length while λ_{max} is computed as per the previous expression except that it is bounded to 20% of the mixed-layer depth.

The friction velocity in the water interior needed in the computation of K_m is determined from the values of u, v, and K_m at the previous time step according to $u_* = \sqrt{K_m \left(u_z^2 + v_z^2\right)^{1/2}}$, where u_z and v_z are vertical shear components for x and y directions, respectively. At the first time step, however, K_m is determined iteratively from a steady version of the equations. Note that this scale velocity is modified by the buoyancy flux in the destabilizing case [see *McPhee*, 2008].

The thermal and haline diffusivities $K_{h,s}$ are related to K_m as

$$K_{h,s}/K_m = \exp\left(-1.5\sqrt{Ri - 0.079}\right), \tag{3}$$

with upper and lower limits of 1 and 0.039, where the gradient Richardson number is $Ri = \frac{N^2}{u_z^2 + v_z^2}$. Therefore, in the strong stably stratified situation (i.e., $N^2 \gg u_z^2 + v_z^2$) as is the case for melting, the heat and fresh-water exchange can be significantly reduced compared to the momentum exchange. This algorithm for determining viscosity and diffusivity has been verified through comparison with simulations using the Mellor and Yamada's turbulent closure scheme [*Mellor and Yamada*, 1982], and validated with observations in the ice-covered seas of the Arctic and Antarctic Oceans [*McPhee*, 1999, 2008].

At the ice-ocean interface, the frictional velocity magnitude u_{*0} is used as the boundary condition for the momentum equation, where u_{*0} is estimated following Rossby's similarity law,

$$\frac{\kappa \mathbf{U_0}}{\mathbf{u_{*0}}} = \frac{1}{\kappa}\left(\log\frac{\mathbf{u_{*0}}}{fz_0} - A - iB\right), \tag{4}$$

where the under-ice surface roughness length z_0 is 0.049 m, and constants A and B are $A = 2.3$ and $B = 2.1$, respectively (these constant values correspond to the neutral case). The value of z_0 highly depends on local conditions. Under ice roughness, length was estimated to be 6 mm for hydraulically smooth ice floes during SHEBA [*McPhee*, 2002]. A more complete assessment from SHEBA data, considering also rougher under ice topography suggests a mean value of z_0 of 0.049 m (used here) and a range of [0.016 m, 0.146 m] [*McPhee*, 2008, chapter 9]. *Shaw et al.* [2008] estimate an average value of 0.1 m from buoys observations in the Arctic. Ice-ocean relative velocity $\mathbf{U_0}$ (here equated to the ice-drift velocity under the assumption of weak ocean flow) and friction velocity $\mathbf{u_{*0}}$ are complex numbers. Here we take Ice-T's velocity as the ice-drift velocity $\mathbf{U_0}$.

The friction velocity is shown in Figure 12 for $z_0 = 0.049$ m, while the grey patch denotes the envelope for z_0 in the interval [0.015 m, 0.15 m]. In the period between DoY 140 and 170, encompassing the three events, u_{*0} is generally less than 0.01 m s^{-1}. The friction velocity is lowest late in Event 3, when u_{*0} falls below 0.005 m s^{-1}, which is substantially smaller than the climatology for May and June in the TPDS region [*Krishfield and Perovich*, 2005]. During this time, the mean array motion is observed to be nearly stationary due to calm weather following a transient cyclone.

Early in Event 3 (DoY 157–161), the buoy array was located in the middle of a well-developed low-pressure system, that centered in the northern Barents Sea and migrated to the east, concurrent with a high-pressure system that lay over the central Beaufort Sea (not shown). The pressure gradient between these disturbances caused substantial northward winds over the array during DoY 156–161. After the low passed away to the southeast toward the Siberian continent between DoY 162 and 168, the array was subsequently dominated by a persistent high-pressure system for almost a week, and subjected to modest wind conditions (not shown).
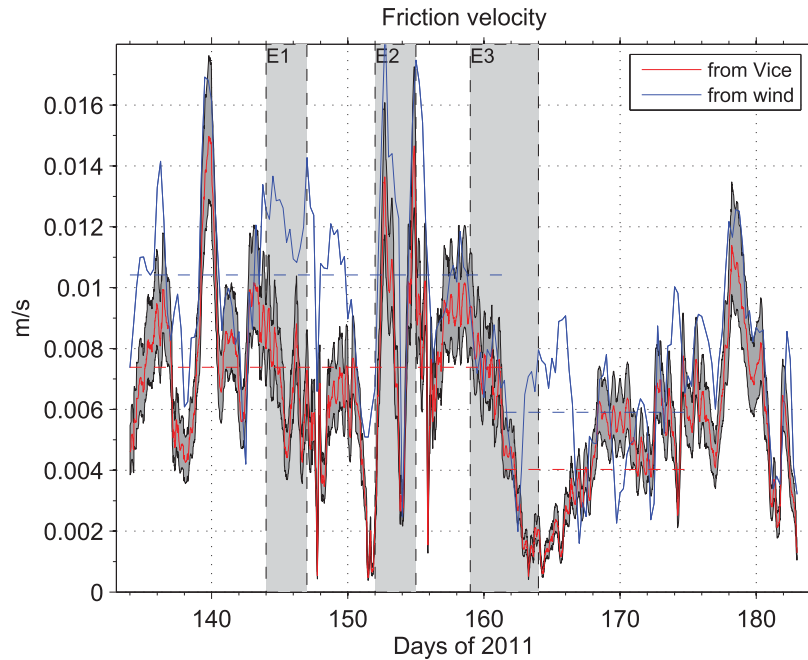
Figure 12. Time series of $|u_{*0}|$, the module of the interfacial friction velocity, which is estimated based on the Rossby's similarity law using the drift velocity derived from Ice-T positions and a roughness length of 0.049 m (red line), while the gray envelope is for $z_0 = [0.015,0.15]$ m. For comparison, the thin blue curve denotes the friction velocity estimated from the 10 m wind speed from ERA-Interim (see equation (5)). The dashed horizontal blue and red lines denote the average of the corresponding friction velocity for the period ranging from DoY 134 to 162 and 162 to 175.

In addition, we display in Figure 12 the friction velocity magnitude derived from the 10 m wind speed U_{10} from ERA-interim, which is applicable to driving the ocean if we assume free ice drift, according to

$$\mathbf{u}_{*a} = \frac{\tau_a}{\sqrt{|\tau_a|}}, \quad \text{with} \quad \tau_a = \frac{\rho_a}{\rho_w} c_{10} \, \mathbf{U}_{10} \, |\mathbf{U}_{10}|, \tag{5}$$

where ρ_a is the density of air, and $c_{10} = 0.002$. These two estimates of the friction velocity, $\mathbf{u}_{*a}$ and $\mathbf{u}_{*0}$, are highly correlated (0.69, significant at >99%). Largest discrepancies occur during Event 1, where u_{*a} exceeds u_{*0} by more than 20%, and at the end of Event 3, when the array is stationary, while u_{*a} is as large as 0.008 m s^{-1}.

5.1.2. Submodel for Heat and Salt Budget at the Ice-Ocean Interface

At the ice-ocean interface, the thermal balance between conductive heat flux in the ice column, turbulent heat flux from the ocean, and latent heat release or absorption from melting or freezing read:

$$-\frac{\dot{q}}{\rho_w c_p} + <w'T'>_0 \; = w_0 \frac{L_{ice}}{c_p}, \tag{6}$$

where $<w'T'>_0$ is the turbulent heat flux from ocean and w_0 is the interface vertical velocity adjusted bottom melt rate (i.e., $w_0 = -\frac{\rho_i}{\rho_w} \dot{h}_{ice}$). In the model, the conductive heat through the ice column is given by the temperature gradient measured closest to the ice bottom (section 3.5, Figure 9). Turbulent heat flux between the ice and ocean is calculated by a bulk formulation [*McPhee*, 2008]:

$$<w'T'>_0 = \alpha_h u_{*0} \, (T_{ff} - T_0) \tag{7}$$

where exchange coefficient for temperature is $\alpha_h = 1.0 \times 10^{-2}$. The interfacial flux is based on the difference between temperature values at the ice-ocean interface (T_0) and far field (T_{ff}) in the water. The far-field temperature, T_{ff}, is that provided by the model at 2 m depth.

The salinity budget at the interface is computed at each model time step in a way similar to that used for heat, i.e.,

$$<w'S'>_0 + w_0 \ (S_i - S_o) = 0, \tag{8}$$

$$<w'S'>_0 = \alpha_s u_{*0} \ (S_{ff} - S_o), \tag{9}$$

where S_i is 5 and S_{ff} is the salinity at 2 m. Here α_s is different from α_h to account for double diffusion across the molecular sublayer under melting ice. It is set at $\alpha_s = \alpha_h/35$, similar to a solar radiative heating experiment in *McPhee* [2008]. An additional relation links T_0 and S_0 to close the system of equations at the interface: it is assumed that T_0 is the freezing temperature $T_f(S_0)$. The submodel solves for S_0 and T_0 and computes temporal changes in ice thickness, w_0, representing growth/decay at the ice base, as well as the buoyancy flux, which is injected in the main boundary layer model.

5.1.3. Solar Heating at Leads

The observational evidence presented in section 3 supports the assumption that solar radiation through leads warmed the upper ocean. Hereafter, we examine in greater detail the impact of lead opening. The sequential web camera images and the buoy array deformation (Figures 4 and 6) indicate that the lead openings occurred adjacent to the instruments during the ice deformation Events 2 and 3. For example, the lead was roughly 10–30 m distant from the buoys during Event 2. In our simulation, we assume that the absorbed heat at all lead surfaces is immediately available under the ice. The heat input from local lead openings, such as that near our instruments, is up-scaled to the region about the instruments using mean ice concentration from satellite observations.

We assume the heat that enters the upper ocean through leads exponentially decays with depth, and the warmed lead water spreads under ice evenly due to diffusive processes or differential motion of the ice and upper ocean. A recent compilation of optical observations by *Aas et al.* [2013] shows that polar waters north of the Svalbard are typically of oceanic type III according to the classification of *Jerlov* [1968], that is much less optically clear than the commonly used type IA. We use the double extinction profile (R) proposed by *Paulson and Simpson* [1977] for type III water to distribute the solar radiation in the upper ocean, which is virtually entirely absorbed in the shallow mixed layer:

$$R(z) = 0.78e^{-z/1.4} + 0.22e^{-z/7.9} \tag{10}$$

Technically, we use the vertical derivative of this expression to use it as a source term in the ML heat equation. To achieve area averaging of heat flux, it is further multiplied by the available shortwave radiation at the lead surface $F_i = (1 - SIC)(1 - a)F_r$, where F_r is the incident shortwave radiation from ERA-interim and where the SIC is also taken from ERA-interim in our reference experiment (see section 4.3 and Figure 10b).

5.2. Simulation Results

The model predicts the ice thickness evolution based on the salt/heat balances at the ice-ocean interface (Figure 13a). The simulated thickness consistently tracks the observed ice thickness detected by the Ice-T's upward looking sonar, which increases up to DoY $\sim$150 and then decreases. While the agreement with observations is excellent at the end of the simulation, the melting rate sharply increases in the model around DoY 167, in the wake of Event 3, enabling it to catch up with observations, whereas observed melting peaks earlier during Event 3.

The simulated ice thickness evolution results from the balance between the conductive heat flux in the ice, used as a forcing of the model, and the turbulent ocean-ice heat flux output by the model. Both are shown in Figure 13b (in negative for the conductive heat flux). The turbulent heat flux exhibits a gradual increase with time, and it is particularly enhanced shortly after Event 3, the maximum being nearly 40 W m^{-2}, which is much higher than climatology, $\sim$7 W m^{-2}, for June in the TPDS region [*Krishfield and Perovich*, 2005]. It is also significantly greater than that measured in the same region during May and June 2010 by POPS#13, which was less than 10 W m^{-2} prior to DoY 165 [*Kawaguchi et al.*, 2012]. Also reproduced in Figure 13b is the available solar radiation used to force the model. Comparison between the turbulent heat flux at the ice-ocean interface and the solar energy at leads indicates that the incident solar energy is most effectively consumed in basal ice melt before and after Event 3 in the simulation, although the greatest solar forcing occurs during Event 3. The contrast is owed to relatively high friction velocity estimated from Event 2 to the beginning of Event 3 (reaching 0.013 m s^{-1} during Event 2), as well as after Event 3, that increases the turbulent heat flux near the ice bottom. The solar energy supply at leads peaks at $\sim$40 W m^{-2} near the end of
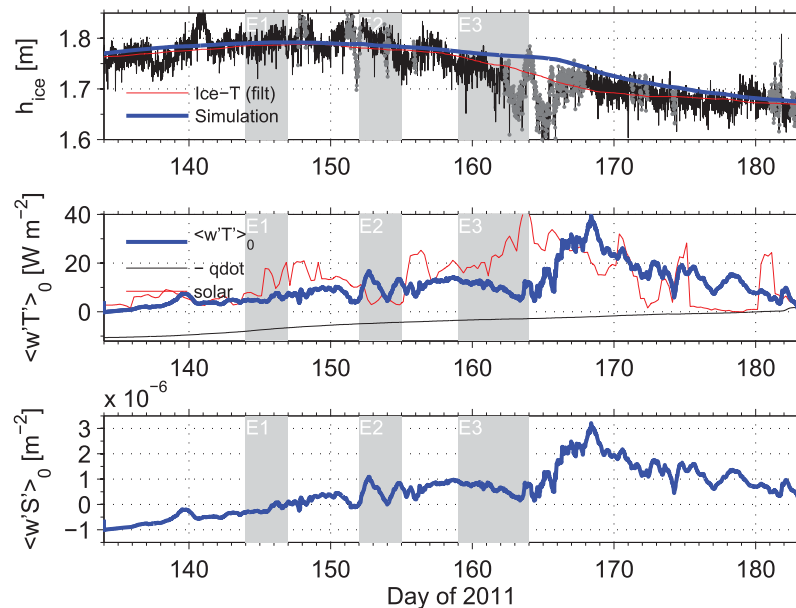
Figure 13. Temporal evolution of (a) ice thickness, (b) turbulent heat flux at the ice-ocean interface, and (c) turbulent salt flux at the inter-face. In Figure 13a, the blue thick curve denotes simulated ice thickness, while black (red) lines are raw (filtered) ice thickness observed from Ice-T (see Figure 8). In Figure 13b, the blue curve is the simulated turbulent heat flux; also shown are the available solar radiation (red) and the negative of the conductive heat flux (black) used to force the model.

Event 3, but only a limited portion is used for ice melt because the very small friction velocity, less than 0.002 m s^{-2}, generates less turbulent mixing under the ice.

The basal salt flux variations shown in Figure 13c mimic those of the turbulent heat flux. It is negative until DoY ~149 due to salt release through ice growth, and is then positive due to melting.

The simulated salinity and temperature in the ML are compared with in situ measurements by Ice-T and POPS (Figures 14a and 14b). Unsurprisingly, as anticipated in section 4.4, the model salinities do not suc-cessfully reproduce observations. Both Ice-T and POPS measurements show a rapid salinity decrease of ~0.4 by the end of Event 3, incommensurate with the observed melting rate. In the model, although the freshwater input due to melting is confined to a shallow sublayer, it leads to a salinity decrease of only ~0.2 later around DoY 172. Observations further show that salinity peaks around DoY 176, increasing from the bottom of the ML, which cannot be explained by the 1-D thermodynamic budget at the surface. The differ-ence between observed and modeled salinity is likely due to horizontal gradients in the upper ocean salin-ity, which are unrelated to the modeled ice-ocean interaction and may be associated with submesoscale disturbances due to the baroclinic instability along the lateral density fronts in the surface layer [*Timmer-mans et al.*, 2012; *Mahadevan et al.*, 2010]. An alternative hypothesis for this increase in salinity near DoY 177 is a deepening of the ML, causing mixing with saltier waters below. The appearance of a surface summer layer (SSL) noted previously in POPS observations (section 3.3; Figure 7), and as will be further dis-cussed below, suggests that the source of mixing may not originate from the surface as deep mixing is inhibited. It could instead be caused by internal ocean dynamics.

The model reproduces much more successfully the observed temperature variations at least up to DoY 165–170 (Figures 14b and 15a). Compared to Ice-T and POPs observations, we see that both the general moderate warming trend from the beginning of the simulation, as well the vertical structure of the warming peak starting at the end of Event 3 are very well reproduced. After that date, the simulated warming appears excessive compared with Ice-T observations. However, we lack full depth observations from POPS until DoY 177 to assess whether this lasting warming pattern is indeed a feature that simply extends below the depth of the Ice-T temperature's sensor, or whether its magnitude is overestimated in the simulation. Regarding the very end of the simulation, after DoY 177, the cooling apparent in observations is crudely reproduced by the model. Previous comments on salinity variations during this period, however, indicate
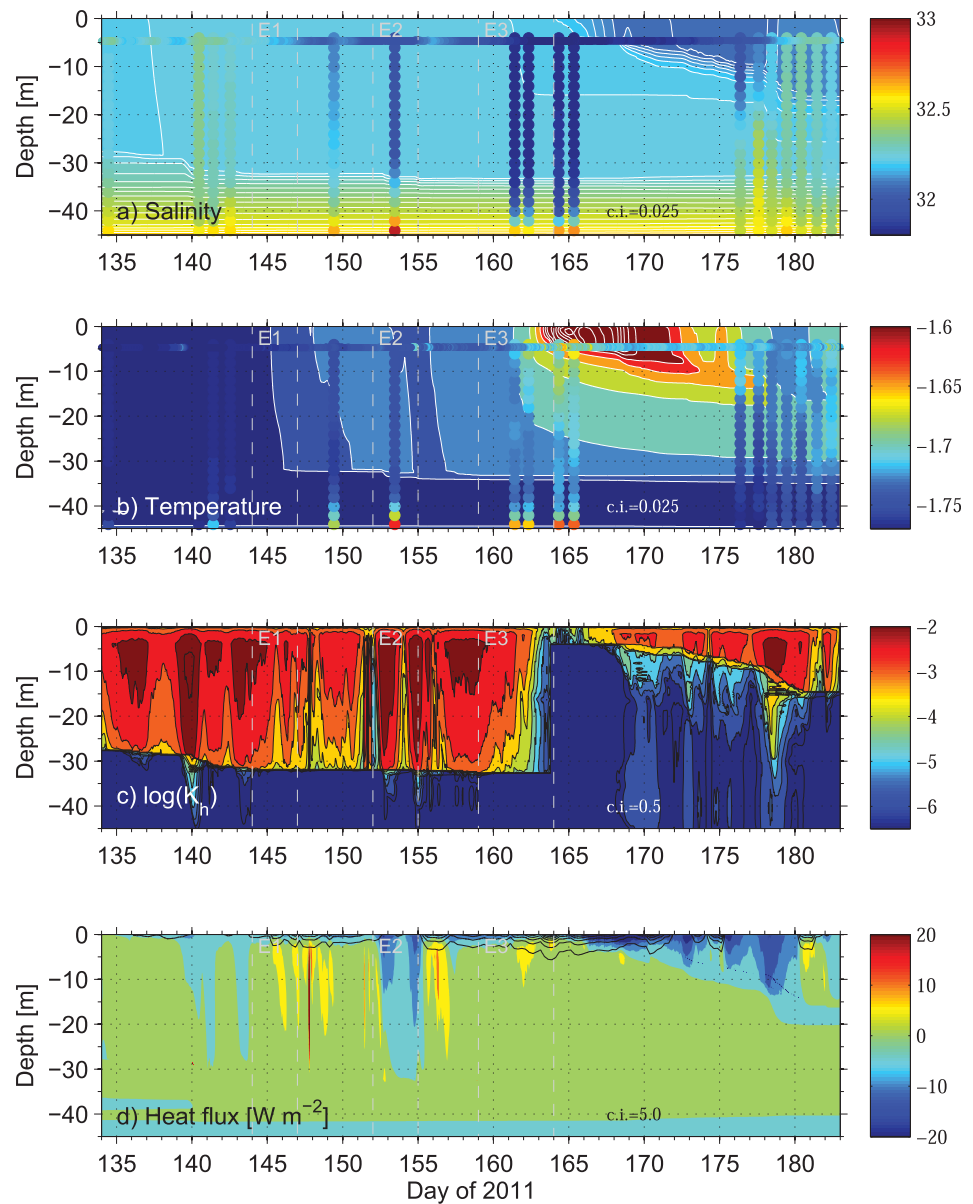
Figure 14. Simulation results using forcings from ERA-interim: (a) salinity, (b) temperature, (c) decimal logarithm of the turbulent heat diffusivity K_h, and (d) vertical turbulent heat flux (color) and radiative heat flux used to force the model (black contours, c.i. = 5 W m^{-2}). In Figures 14a and 14b, observations from Ice-T and POPS are superimposed.

that other mechanisms, not included in the model, might be at play. We will therefore disregard hereafter this part of the simulation.

We can explore the dynamics behind temperature changes within the ML by examining the evolution of the simulated density stratification, turbulent viscosity, and vertical heat flux. During the early simulation period until DoY 163, encompassing Events 1 and 2 and the start of Event 3, the temperature is well mixed above 30 m (Figure 14b). Temperature increases by ∼0.03 K at maximum for both events. In the upper level, where warming takes place, the density stratification is small, $N^2 = 3 \times 10^{-7} \text{s}^{-2}$ on average (not shown). At the bottom of the well-mixed upper layer, ∼30 m depth, stratification is maximum ($N^2 = O(10^{-4})$ s^{-2}) which impedes the turbulent energy at the interface from being transferred to lower depths.

During this period, the turbulent mixing, which may be represented by the eddy viscosity K_m, is strong, 1.4×10^{-3} m^2 s^{-1} on average in the upper layer, where the friction velocity is $u_{*0} = 0.0073$ m s^{-1}. Although
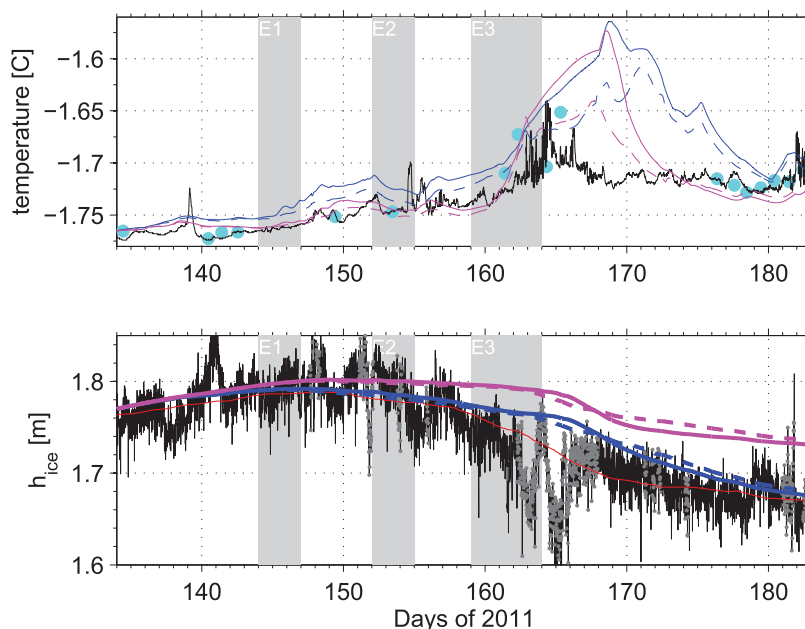
Figure 15. Time series of (a) temperature and (b) ice thickness from Ice-T observations (black line) and from different simulations at the corresponding vertical level of the model. The blue solid line is from the reference experiment forced by ERA-interim SIC. The magenta line is from a sensitivity experiment forced by AMSR SIC. Dashed blue and magenta lines are the results of the corresponding simulations forced by the friction velocity based on the wind stress instead of the IceT-buoy's drift velocity (see blue line in Figure 12). In Figure 14a, cyan dots denote the temperature observed by POPS at the same depth as the Ice-T.

large, this estimate of K_m remains 1–2 order or magnitude smaller than the values measured in the Chukchi Sea for ice-free conditions [*Kawaguchi et al.*, 2015]. The eddy viscosity is not shown, but we display instead the thermal diffusivity K_h in Figure 14c, whose variations mimic those of K_m. According to (3), the ratio of diffusivity to eddy viscosity cannot exceed unity, reflecting that turbulence transfers momentum at depth more efficiently than scalar properties. The dependence on Ri in (3) indeed implies that K_h decreases more rapidly with depth than K_m. However, their magnitudes are identical in the upper 30 m until DoY 163 owing to a small Ri associated with the weak stratification.

Note that the simulated K_h is approximately a factor of 3 greater than the magnitude estimated from microstructure measurement under the ice as reported in *Sirevaag et al.* [2011] in the central Amundsen basin (87.5°N) in August 2008. They evaluate 3.7×10^{-4} m^2 s^{-1} for the average eddy diffusivity in the upper mixed layer, consistent with a smaller friction velocity of $u_{*0} = 0.0026$ m s^{-1}. According to the simulation, the surface turbulence does not deepen the main pycnocline of the WML, located around 40–50 m, which is consistent with the observation of *Sirevaag et al.* [2011].

Figure 14d depicts how the model simulates the turbulent heat flux throughout the mixed layer. The solar heat flux penetrating the mixed layer is also indicated in this figure by black contour lines (every 5 W m^{-2}), showing that it is mainly confined to the upper 5 m. The turbulent mixing excited by the ice-ocean stress during the beginning of the simulation effectively transports the solar energy absorbed near the surface downward, which finally produces well-mixed properties for the water column. By contrast, during the second half of Event 2 when the energy input at leads almost vanishes, according to the available solar forcing used in the simulation, the u_{*0}-induced turbulent mixing keeps working at homogenizing the ML hence cooling the upper levels. The ocean-ice heat flux is nevertheless persistently upward, provided by the heat storage in the ML (Figure 13b).

The period in the wake of Event 3 is characterized in the simulation by the enhanced warming and freshening within a very shallow surface layer, corresponding to the SSL. The observations also indicate shallow warming but to a lesser degree. Starting in the middle of Event 3, temperature elevation is most apparent, exceeding 0.2 K near the surface after a few days within a notably thin layer, ∼7m. Below this layer, temperature decreases rapidly with depth, instead of being uniform as previous to Event 3 (Figure 14b). Freshening

takes place within the near-interface thin layer, where salinity reduces by >0.1 five days after the end of the event (Figure 14a). Freshening does not reach below this thin layer.

During Event 3, there was significant attenuation in interfacial friction velocity, where $u_{*0}=0.001-0.003$ m s^{-1} (Figure 12). This is also when substantial solar energy was persistently absorbed at the leads, with magnitude reaching 40 W m^{-2} on DoY 164 (Figure 10b or Figure 13b). The combination of these two factors led to the development of the shallow temperature anomaly promoting ice melting and associated freshwater input at the surface that reinforced stratification. The turbulent heat flux calculated in the model indicates that the vertical heat transfer was drastically inhibited below the SSL that developed (Figure 14d). Another consequence of the formation of the SSL is that the buoyant meltwater remains near the interface, instead of being transferred downward (Figure 14a). With ice-ocean stress increasing up to $u_{*0}=0.007$ m s^{-1}, the thin SSL then begins to thicken through entrainment (Figures 12 and 14c) about DoY 178. The increasing mixing starts to erode the shallow stratification, yielding a negative turbulent heat flux (Figure 14d) which contributes to cooling the topmost layer so that the temperature anomaly remains only persistent in the subsurface, between 10 and 20 m, underlying the near-surface halocline (Figure 14b). This is consistent with the initial formation of a near-surface temperature maximum (NSTM) as reported by *Jackson et al.* [2010].

Mellor et al. [1986] discuss the stabilizing effects of meltwater on turbulent mixing in the mixed layer using the *Mellor and Yamada*'s [1982] second-order turbulent closure model. In their simulation, they compare two cases when warm surface water melts overlying sea ice with and without wind forcing. Their simulation shows that for the wind-imposed case, the ice-ocean interfacial shear stress works to reduce the stabilizing effects due to the meltwater. This is consistent with the results of our simulation: while during Events 1 and 2, when ice ocean stress is relatively strong, deeper mixing enables storage of thermal energy absorbed in leads throughout the ML, in the wake of Event 3, the stabilized surface layer prevents vertical exchange of heat and salt.

The POPS temperature and salinity profiles document the establishment of the fresh and warm SSL. This SSL is 20–25 m deep around DoY 198 and becomes deeper with increased stratification until the DoY 226 profile (Figure 7). There is evidence of a SSL in the profiles available around DoY 177, but it seems transient and subsequently eroded between DoY 180 and 190, with a deepening of the ML. Therefore, the simulated SSL in the wake of Event 3 may only be the precursor of a robust surface layer. *Toole et al.* [2010] tried to quantify typical depth of the early-summer SSL, using ship-based hydrography data and found it is generally less than 10 m, which is consistent with our 1-D model simulation.

5.3. Sensitivity of the Results

The analysis of the upper ocean's heat budget and ML dynamics presented above is based on one model simulation. As seen in section 4, however, there are substantial uncertainties both in the radiative forcing (SIC and shortwave flux are not accurately known) and the mechanical forcing (the friction velocity for instance depends on the roughness length z_0, a parameter which we can only guess). To assess the robustness of the results based on the reference simulation, we have run different experiments, varying the forcing field. First the reference experiment was modified to change the friction velocity only. Under the assumption of free drift, we equated u_{*a} (blue line in Figure 12) and u_{*0} for this run. It is thus an upper bound that enables us to test the robustness of the SSL. While u_{*a} is well correlated with u_{*0} and generally falls within the envelope of u_{*0} for a physically realistic range of z_0, it far exceeds u_{*0} most notably at the end of Event 3 (DoY 163–167), when the buoy array is virtually motionless.

The simulated temperature at the depth of the Ice-T sensor is shown in Figure 15a, whereas the ice thickness is shown in Figure 15b. Compared to the reference experiment (reproduced in blue), the simulation forced by u_{*a} (dashed blue) shows a slightly better agreement in the melting rate, and most notably, a better agreement with the observed temperature at 7 m. Deep mixing occurs between DoY 163 and 168, contrary to the reference run, which enhances surface melting, and spreads downward the radiative warming (not shown). A SSL nevertheless builds up as in the reference experiment. The subsurface temperature maximum is more spread out and has a consequently smaller amplitude. However, similar to u_{*0}, there is a stark contrast in the intensity of the wind-based forcing before and after DoY 162: the average intensity for the period DoY 162–175 is almost half that for the period prior to DoY 162 (dashed line in Figure 12), and is also 20% smaller than the average intensity of u_{*0} prior to DoY 162. Therefore, although forcing is substantially

increased in this sensitivity run, the period in the wake of Event 3 can still be considered as relatively quiescent compared to the period before.

Another set of experiments considered different radiative forcing, using instead SIC from AMSR rather than ERA-interim (shown in Figure 10b). As previously, two separate simulations were carried out: one forced with u_{*0}, as for the reference run, and one forced by u_{*a} (solid and dashed magenta line, respectively, in Figure 15). The available solar radiation based on AMSR SIC is consistent but in general smaller than that computed using SIC from ERAI (Figure 10b), which explains the poorer agreement with observations for the ice thickness evolution (Figure 15b). The evolution of the temperature field is qualitatively similar to that of the reference simulation, with a temperature peak of shorter duration, however, due to the vanishing available solar forcing due to the increase in SIC after DoY 170 (Figures 10b and 15a). Imposing enhanced mechanical forcing with u_{*a} does not prevent the formation of a SSL as in the reference run. Its effect is, as previously, to spread vertically, and thus reduce the magnitude of the temperature peak.

Finally, we performed additional sensitivity runs, whereby we varied several parameters of the model, in particular the temperature and salinity exchange coefficients α_h and α_s, respectively, while remaining in the range of value prescribed by *McPhee* [2008]. The impact of such changes on the results is comparatively much weaker than that associated with the different forcings used above. As forcing is the main source of uncertainty, the boundary layer model coefficients are not discussed further.

6. Summary

At an autonomous drifting station in the central Arctic Ocean, deployed at the NPEO, we conducted observations of a variety of parameters such as ice motion, divergence, and temperature and salinity profiles of the ice and ocean mixed layer, using a combined system of multiple sensors during the transition from cold spring to early summer. Over the observation period increasing temperature was observed in the upper ocean and the onset of basal melt occurred in mid-May, 20 days before surface melt. We estimate that about 17 W m^{-2} of heat input to the upper ocean is required for the observed warming and melt (85% of the heat flux was consumed by melting). Our ice-motion measurements using GPS drifters that were initially placed to form a cluster with 7 km side length captured three distinct deformation events. During each event, ridging was followed by lead opening. Satellite sea ice concentration observations suggest that locally observed lead openings were part of a larger-scale pattern. Ridges and leads were observed to form 10–30 m from the site where ice and ocean profiles were recorded during Events 2 and 3. Temperature spikes were observed at 6 m below the ice during these two events, which appear to coincide with the timing of lead opening. It is unlikely that 17 W m^{-2} could have been provided by oceanic upwelling. Rather, after DoY 136, absorption of solar radiation through leads provides sufficient heat to the upper ocean to explain the warming and melt, given that milder atmospheric conditions prevent refreezing at leads, as evidenced from an examination of the surface energy budget (section 4.3).

A 1-D turbulent closure model was used to analyze how solar input at leads and ice drift control upper ocean stratification and heat flux to the ice. This model was forced by the solar heat flux through leads using sea ice concentration and shortwave radiation from ERA-interim reanalyses (assuming the input through leads was immediately available at the measurement site under the ice), by the measured conductive heat flux through the ice, and by the observed drift velocity. The simulation was started on DoY 136 when solar heat flux through leads was shown to be the dominant term of the surface energy budget. This period thus captured the final phase of ice growth and the beginning of basal melt and included in particular the three deformation events documented by observations.

Event 3, in contrast to previous events, saw a reduced turbulent mixing due to low ice motion. The model results indicate that during Event 3 reduced kinetic mixing and enhanced heating from solar radiation near the ocean surface resulted in the buildup of a shallow stratification. This shallow warm layer promoted upward heat flux to the ice and basal melt as soon as friction velocity picked up in the wake of Event 3. During Event 2, by contrast, vertical heat flux to the ice was about a factor of two lower, in part because solar warming was not as strong, but mainly because a larger friction velocity resulted in deeper mixing. The quiescent conditions with lead opening as the ice pack relaxed following a ridging event (Event 3) may have been the precursor to the formation of the summer surface layer (SSL).

The dependence of ocean heat flux on ice concentration and ice motion cause spatial and temporal heterogeneity in this flux. *Hayes and Morison* [2008] demonstrated that spatial heterogeneity in ocean heat flux to the ice is related to ice friction velocity, roughness length (under-ice topography), and, prior to ice becoming permeable, the size and distribution of leads. Similar to our findings, they recorded quiescent conditions in mid-summer resulted in retention of meltwater near the surface. This accumulation and subsequent release to the mixed layer impacts the timing of heating of the ice base and volume of lateral and basal ice melt. We hypothesize that variability in ice motion and lead opening controls the large spatial heterogeneity in ocean heat flux to the ice base during spring and early summer, while the surface fresh layer is forming. Understanding the relative importance of each, such that a parameterization of heat flux can be developed based on the history of wind stress and ice mechanical response, would be aided by 3-D modeling of the mixed layer and ice that allows for lateral mixing. Such efforts benefit from field experiments with spatial sampling of the mixed-layer temperature and salinity together with surveys of the ice thickness field [e.g., *Hayes and Morison*, 2008].

In this paper, it is demonstrated that even before ice surface melt commences, lead opening can result in basal ice melt when mild atmospheric conditions prevent refreezing.

Our observations near the North Pole contrast with those analyzed by S. G. Gallaher et al. (Evolution of a Western Arctic ice-ocean boundary layer and mixed layer across a developing thermodynamically forced Marginal Ice Zone, submitted to *Journal of Geophysical Research*, 2016) in the Beaufort Sea ∼1700 km further south in 2014, which show that melt pond drainage initiated the near-surface stratification that enabled basal ice melt to pick up. Both studies agree, however, in showing that the observed ice melt and ML warming rates can be reasonably well accounted for by a 1-D budget considering solar forcing and ice concentration on spatial scales on the order of 50–100 km. Leads open in response to wind stress over the ice pack. Hence, the onset of basal ice melt and solar warming of the mixed layer is controlled by the synoptic variability of the atmosphere, and we expect the timing of basal melt onset is as variable as the timing of surface melt onset.

References

Aas, E., N. K. Højerslev, J. Høkedal, and K Sørensen (2013), Optical water types of the Nordic Seas and adjacent areas, *Oceanologia*, *55*(2), 471–482, doi:10.5697/oc.55-2.471.

Cogley, J. G. (1979), The albedo of water as a function of latitude, *Mon. Weather Rev.*, *107*, 775–781.

Fairall, C. W., E. F. Bradley, D. P. Rogers, J. B. Edson, and G. S. Young (1996), Bulk parameterization of air-sea fluxes for Tropical Ocean-Global Atmosphere Coupled-Ocean Atmosphere Response Experiment, *J. Geophys. Res.*, *101*(C2), 3747–3764, doi:10.1029/95JC03205.

Fung, I. Y., D. E. Harrison, and A. A. Lacis (1984), On the variability of the net longwave radiation at the ocean surface, *Rev. Geophys.*, *22*(2), 177–193, doi:10.1029/RG022i002p00177.

Hayes, D. R., and J. Morison (2008), Ice-ocean turbulent exchange in the Arctic summer measured by an autonomous underwater vehicle, *Limnol. Oceanogr.*, *53*(5), 2287–2308.

Hutchings, J. K., P. Heil, A. Steer, and W. D. Hibler (2012), Subsynoptic scale spatial variability of sea ice deformation in the western Weddell Sea during early summer, *J. Geophys. Res.*, *117*, C01002, doi:10.1029/2011JC006961.

Jackson, J. M., E. C. Carmack, F. A. McLaughlin, S. E. Allen, and R. G. Ingram (2010), Identification, characterization, and change of the near-surface temperature maximum in the Canada Basin, 1993–2008, *J. Geophys. Res.*, *115*, C05021, doi:10.1029/2009JC005265.

Jerlov, N. G. (1968), *Optical Oceanography*, 194 pp., Elsevier, Amsterdam.

Jin, Z., T. P. Charlock, W. L. Smith Jr., and K. Rutledge (2004), A parameterization of ocean surface albedo, *Geophys. Res. Lett.*, *31*, L22301, doi:10.1029/2004GL021180.

Kawaguchi, Y., J. K. Hutchings, T. Kikuchi, J. H. Morison, and R. A. Krishfield (2012), Anomalous sea-ice reduction in the Eurasian Basin of the Arctic Ocean during summer 2010, *Polar Sci.*, *6*, 39–53.

Kawaguchi, Y., S. Nishino, and J. Inoue (2015), Fixed-point observation of mixed layer evolution in the seasonally ice-free Chukchi Sea: Turbulent mixing due to gale winds and internal gravity waves, *J. Phys. Oceanogr.*, *45*, 836–853, doi:10.1175/JPO-D-14-0149.1.

Kikuchi, T., J. Inoue, and D. Langevin (2007), Argo-type profiling float observations under the Arctic multiyear ice, *Deep Sea Res., Part I*, *54*, 1675–1686, doi:10.1016/j.dsr.2007.05.011.

Krishfield, R. A., and D. K. Perovich (2005), Spatial and temporal variability of oceanic heat flux to the Arctic ice pack, *J. Geophys. Res.*, *110*, C07021, doi:10.1029/2004JC002293.

Mahadevan, A., A. Tandon, and R. Ferrari (2010), Rapid changes in mixed layer stratification driven by submesoscale instabilities and winds, *J. Geophys. Res.*, *115*, C03017, doi:10.1029/2008JC005203.

Markus, T., J. C. Stroeve, and J. Miller (2009), Recent changes in Arctic sea ice melt onset, freezeup, and melt season length, *J. Geophys. Res.*, *114*, C12024, doi:10.1029/2009JC005436.

Maykut, G. A., and M. G. McPhee (1995), Solar heating of the Arctic mixed layer, *J. Geophys. Res.*, *100*(C12), 24,691–24,703.

Maykut, G. A., and N. Untersteiner (1971), Some results with a time-dependent thermodynamic model of sea ice, *J. Geophys. Res.*, *76*(6), 1550–1575.

McPhee, M. G. (1999), Scales of turbulence and parametrization of mixing in the ocean boundary layer, *J. Mar. Syst.*, *21*, 55–65, doi:10.1016/S0924-7963(99)00005-6.

McPhee, M. G. (2002), Turbulent stress at the ice/ocean interface and bottom surface hydraulic roughness during the SHEBA drift, *J. Geophys. Res.*, *107*(C12), 8037, doi:10.1029/2000JC000633.

McPhee, M. G. (2008), *Air-Ice-Ocean Interaction—Turbulent Ocean Boundary Layer Exchange Processes*, 215 pp., Springer-Verlag, N. Y., doi: 10.1007/978-0-387-78335-2.

McPhee, M. G., R. Kwok, R. Robin, and M. Coon (2005), Upwelling of Arctic pycnocline associated with shear motion sea ice, *Geophys. Res. Lett.*, *32*, L10616, doi:10.1029/2004GL021819.

Mellor, G. L., M. G. McPhee, and M. Steele (1986), Ice-water turbulent boundary layer interaction with melting and freezing, *J. Phys. Oceanogr.*, *16*, 1829–1846.

Mellor, G. L., and T. Yamada (1982), Development of a turbulence closure model for geophysical fluid problems, *Rev. Geophys.*, *20*(4), 851–875.

Morison, J. H., et al. (2002), North pole environmental observatory delivers early results, *EOS Trans. AGU*, *83*(357), 360−361.

Paulson, C. A., and J. J. Simpson (1977), Irradiance measurements in the upper ocean, *J. Phys. Oceanogr.*, *7*, 952–956.

Pegau, W. S., and C. A. Paulson (2001), The Albedo of Arctic leads in summer, *Ann. Glaciol.*, *33*, 221–224.

Perovich, D. K. (2005), On the aggregate-scale partitioning of solar radiation in Arctic sea ice during the Surface Heat Budget of the Arctic Ocean (SHEBA) field experiment, *J. Geophys. Res.*, *110*, C03002, doi:10.1029/2004JC002512.

Perovich, D. K., T. C. Grenfell, B. Light, and P. V. Hobbs (2002), Seasonal evolution of the albedo of multiyear Arctic sea ice, *J. Geophys. Res.*, *107*(C10), 8044, doi:10.1029/2000JC000438.

Perovich, D. K., J. A. Richter-Menge, K. F. Jones, and B. Light (2008), Sunlight, water and ice: Extreme Arctic sea ice melt during summer of 2007, *Geophys. Res. Lett.*, *35*, L11501, doi:10.1029/2008GL034007.

Perovich, D. K., J. A. Richter-Menge, K. F. Jones, B. Light, B. C. Elder, C. Polashenski, D. Laroche, T. Markus, and R. Lindsay (2011), Arctic sea-ice melt in 2008 and the role of solar heating, *Ann. Glaciol.*, *52*(57), 355–359.

Price, J., R. Weller, and R. Pinkel (1986), Diurnal cycling: Observations and models of the upper ocean response to diurnal heating, cooling and wind mixing, *J. Geophys. Res.*, *91*(C7), 8411–8427, doi:10.1029/JC091iC07p08411.

Pringle, D. J., H. Eicken, H. J. Trodahl, and L. G. E. Backstrom (2007), Thermal conductivity of landfast Antarctic and Arctic sea ice, *J. Geophys. Res.*, *112*, C04017, doi:10.1029/2006JC003641.

Richter-Menge, J. A., D. K. Perovich, B. C. Elder, K. Claffey, I. G. Rigor, and M. Ortmeyer (2006), Ice mass-balance buoys: A tool for measuring and attributing changes in the thickness of the Arctic sea-ice cover, *Ann. Glaciol.*, *44*, 205–210.

Shaw, W. J., T. P. Stanton, M. G. McPhee, and T. Kikuchi (2008), Estimates of surface roughness length in heterogeneous under-ice boundary layers, *J. Geophys. Res.*, *113*, C08030, doi:10.1029/2007JC004550.

Shaw, W. J., T. P. Stanton, M. G. McPhee, J. H. Morison, and D. G. Martinson (2009), Role of the upper ocean in the energy budget of Arctic sea ice during SHEBA, *J. Geophys. Res.*, *114*, C06012, doi:10.1029/2008JC004991.

Sirevaag, A., S. de la Rosa, I. Fer, M. Nicolaus, M. Tjernstrom, and M. G. McPhee (2011), Mixing, heat fluxes and heat content evolution of the Arctic Ocean mixed layer, *Ocean Sci.*, *7*, 335–349.

Spreen, G., L. Kaleschke, and G. Heygster (2008), Sea ice remote sensing using AMSR-E 89 GHz channels, *J. Geophys. Res.*, *113*, C02S03, doi: 10.1029/2005JC003384.

Stanton, T. P., W. J. Shaw, and J. K. Hutchings (2012), Observational study of relationships between incoming radiation, open water fraction, and ocean-to-ice heat flux in the Transpolar Drift: 2002–2010, *J. Geophys. Res.*, *117*, C07005, doi:10.1029/2011JC007871.

Steele, M. (1992), Sea ice melting and floe geometry in a simple ice-ocean model, *J. Geophys. Res.*, *97*(C11), 17,729–17,738.

Timmermans, M.-L., A. Proshutinsky, R. A. Krishfield, D. K. Perovich, J. A. Richter-Menge, T. P. Stanton, and J. M. Toole (2011), Surface freshening in the Arctic Ocean's Eurasian Basin: An apparent consequence of recent change in the wind-driven circulation, *J. Geophys. Res.*, *116*, C00D03, doi:10.1029/2011JC006975.

Timmermans, M.-L., S. Cole, and J. Toole (2012), Horizontal density structure and restratification of the Arctic Ocean surface layer, *J. Phys. Oceanogr.*, *42*, 659–668.

Toole, J. M., M.-L. Timmermans, D. K., Perovich, R. A., Krishfield, A. Proshutinsky, and J. A. Richter-Menge (2010), Influences of the ocean surface Mixed Layer and Thermohaline stratification on the Arctic Sea Ice in the Central Canada Basin, *J. Geophys. Res.*, *115*, C10018, doi: 10.1029/2009JC005660.